Low-dimensional polariton Fluids : spatial correlation properties and thermodynamics

Emilien Durupt

Communauté
UNIVERSITÉ Grenoble Alpes

THÈSE

Pour obtenir le grade de

DOCTEUR DE la Communauté UNIVERSITÉ GRENOBLE ALPES

Spécialité : **Physique**

Arrêté ministériel : 7 Août 2006

Présentée par

Emilien Durupt

Thèse dirigée par **Régis André**
et codirigée par **Maxime Richard**

préparée au sein **de l'institut Néel**
et de **L'école doctorale de Physique**

Fluides polaritoniques de basse dimensionnalité : propriétés de correlations spatiale et thermodynamique.

Thèse soutenue publiquement le **11 Septembre 2015**,
devant le jury composé de :

Mr, Jean Michel Gerard
Directeur de recherche CEA-INAC, Président

Mr,Joel Leymarie
Professeur, université Blaise Pascal, Clermont-Ferrand, Rapporteur

Mr, Gerace Dario
Professeur Université de Pavie, Rapporteur

Mr, Jesus Zuniga-Perez
Chargé de recherche de premiÃ¨re classe, CNRS CHREA, Examinateur

Mr, Régis André
Directeur de recherche de deuxiéme classe, CNRS Institut Néel, Directeur de thèse

Mr, Maxime Richard
Chargé de recherche de première classe, CNRS Institut Néel, Co-Directeur de thèse

---

"A mon fils à venir, à ton petit frére ou ta petite sœur , à votre maman, à mes parents, à ma famille"

—

Remerciements

Il ne me sera pas possible de remercier l'ensemble des personnes qui de près ou de loin ont contribué à ce travail. Deux personnes néanmoins méritent une attention particulière. Maxime Richard mon directeur de thèse, sans la constance de son soutien je n'écrirais pas ces lignes qui marquent la fin de cette aventure. Max, à tout moment j'ai pu compter sur toi, j'ai pu apprendre de ta rigueur et de tes conseils, je te remercie chaleureusement, je ne te remercierai jamais assez. Régis André, mon directeur officiel, qui a fait bien plus que de jouer le rôle administratif de sa mission et dont les encouragements incessants m'ont soutenu jusqu'à la date de ma soutenance. En parallèle je tiens à remercier l'ensemble des chercheurs et doctorants de l'équipe NPSC et plus largement de l'institut Néel, en particulier Henri Mariette qui m'a chaleureusement accueilli au sein de l'équipe, Gilles Nogues pour les nombreux débats scientifiques, aéronautiques et... pour la tentative de vol ensemble compromise par un avion sans radio. Lucien Besombe pour les discussions endiablées et David Ferrand, mon prof de master qui m'a fait aimer les matériaux semi-conducteurs. Une pensée particulière me vient pour mes collègues et amis, Aurélien Trichet, mon prédécesseur en thèse avec Maxime, François, dit "Prof", Médard et Sebastian Klembt (sicher, meiner schwartzer...), Samir et Claire avec une pensée toute spéciale à Alberto Artioli mon voisin de bureau(de haute lutte, n'est-ce pas ?) qui est devenu Papa avant moi et à Natascia et à Quentin Mermillod, mon voisin de manip. Quentin, je me souviendrai longtemps de nos discussions parlant de montagne et... d'avalanches! Je tiens aussi à remercier les personnes ayant collaboré directement à ce travail : Torsten Klein et Karsten Kruse qui ont été les orfévres de nos micro-cavités, Anna Minguzzi et Sanjoy Datta pour les réunions hebdomadaires entre les côtés expérimentaux et théoriques du projet. L'ensemble des contributeurs à la mise en place et à la réalisation de nos manips : Christophe Bouchard, Laurent Del Rey, Julien Jarreau. Merci de plus à tous ceux que j'oublie.

Enfin, je n'aurais pas tenu le coup durant ces années sans les amis, amies et potes de tous genres les Kika, Milie, Erwan (et oui dix ans vieux frére) Simon, Sebastien, Flo, tit pit, Bobo, Pam, Alex. Pour finir, je tiens à remercier mes parents, mom frères et mes sœur, Mika, Amandine et Cindy, qui m'ont toujours soutenus d'une manière indéfectible et Clélia, ma merveille et la maman de mon fils à venir qui non contente de me soutenir a encaissé sans broncher les longues soirées de solitude lorsque je couchais les pages qui suivent sur le papier.

Contents

1 Determination of the spatial coherence of a ZnO microwire quantum degenerate one dimensional gas of polaritons **4**

1.1 motivations . . . 5
1.2 state of the art on strong coupling regime in ZnO microstructures . . . 7
1.2.1 Short review of strong coupling regime in ZnO-based microcavities 7
1.2.2 Quantum degenerates Bose gases in ZnO structures . . . 8
1.3 Introduction to the strong coupling regime in ZnO microwires . . . 8
1.3.1 Short introduction to the strong coupling regime in semiconductors 9
1.3.2 Zinc Oxide : a large bandgap semiconductor . . . 13
1.3.3 ZnO microwires structural properties and growth process . . . 17
1.3.4 Optical properties of ZnO microwires . . . 17
1.4 One dimensional Zinc Oxide Polariton spectroscopy . . . 21
1.4.1 Non-resonant injection . . . 22
1.4.2 Fourier Spectroscopy . . . 24
1.4.3 Linear properties . . . 28
1.4.4 ZnO polariton laser properties . . . 32
1.4.5 Coherence properties of the one dimensional polariton laser . . . 36
1.4.6 Driven dissipatitive mean field model simulation . . . 40
1.4.7 Conclusion on the coherence properties of the measured one dimensional highly excitonic polariton condensate . . . 44
1.5 Applications/ouverture : polariton application . . . 46
1.6 Conclusion . . . 47

2 Using polariton as a coolant in 2D planar micro cavity **48**

2.1 Introduction . . . 48
2.1.1 Generalities on Anti-Stokes Fluorescence cooling in solid state environment . . . 49

2.2 Polariton Anti Stokes Fluorescence cooling 51
2.2.1 Polariton advantages in the context of ASF cooling 51
2.3 Sample 52
2.3.1 cavities fabrication 52
2.4 Experimental setup 57
2.4.1 Injection 57
2.4.2 Detection filtering 59
2.4.3 Detection probability 60
2.5 Typical ASF spectrum and polariton ASF involved mechanisms 60
2.5.1 Polarization properties of the polariton anti-Stokes fluorescence . 65
2.6 Measurement of the thermal fluxes 69
2.6.1 Experimental method to count the extracted phonons 70
2.6.2 Determination of the thermal balance : 73
2.6.3 Quantitative analysis of the thermal fluxes versus temperature. . . 75
2.7 conclusion 77
2.8 perspectives 77

Bibliography **83**

Introduction

The light-Matter interaction has attracted the scientists interest since more than one century : after its first observation by Alexandre Edmond Becquerel in 1839 [1] the photoelectric effect has been theoretically understood by Einstein in 1905 [2]. During the last century our knowledge about the light and its interaction with the matter increased. Using another second prediction of Einstein : the stimulated emission [3], the laser : a new device was experimentally demonstrated by Theodore Maiman in 1960 [4]. This device opened, among other things, the way to optical cooling of atoms which allowed the experimental realization [5, 6] of a third theoretical prediction of Albert Einstein : the Bose Einstein condensation (BEC) [7, 8].

The objects studied in this thesis, the exciton-polaritons, are resulting from the light-matter interaction in the strong coupling regime which consists in a coherent and reversible exchange of energy between matter (atoms, excitons) and the photonic field. This regime has been observed in 1983 in atoms [9] and in semiconductor materials [10]. Exciton polaritons are mixed exciton-photon states. Since polaritons are composed of two bosons, they feature a bosonic character and at low enough density, they are constituting a Bose gas. Their intrinsic half light, half matter nature makes them very well suited particles to investigate dissipative Bose gases in solid state environment. Polaritons inherit their very low effective mass and their short lifetime from their photonic part and are featuring the interacting character of an exciton gas. With those characteristics, polaritons interact with their environment. By tuning the energy difference between the photonic and excitonic parts of the polaritons one is able to modify at wish their photon-exciton ratio and thus to modify the effective mass of the polaritons, the interaction strength between the polariton themselves but also with the lattice vibrational excitations called phonons.

This work is devoted to the study of the interaction of a Bose gas of polariton with its environment it aims to determine the impact of the gas density, the dimensionality

of the confinement, the experienced potential and the surrounding phonon bath on the polariton Bose gas characteristics.

The first part of this work is devoted to the study of a quantum degenerate gas of polariton. The quantum degenerate regime consists in the macroscopic occupation of the ground state of a system of bosons. The key characteristic of this regime is the spontaneous formation of a coherent phase in the system. It has been observed already for polaritons with the experimental demonstration of BEC [11] in 2006 and excitons in 2012 [12]. In this chapter, we study a one dimensional polariton condensate in Zinc Oxide microwires that features a quasi excitonic nature. By determining the spatial correlation properties of the gas, and using a mean field driven dissipative model developed by our colleagues of the Laboratoire de Physique et de Modélisation des Milieux Condensés we were able to determine the influence of the combined quasi excitonic nature, disordered one dimensional confining potential and density on the coherence properties of the gas. The end of the chapter describes an application of those highly excitonic polaritons to a novel subwavelength imaging technic based on the Solid Immersion Lens concept.

In the second part we address the interactions of the polariton field with an intrinsic characteristic of the solid state environment : the thermal excitations of the lattice called phonons. In this part, we use angle resolved Raman spectroscopy to study Anti-Stokes Fluorescence (ASF) which consists in the the absorption of a phonon by an excited states to cool down the studied microcavity. The state of the art technics are using ion doped materials [13] or bare excitons in semiconductors [14] as emitters. The study performed exploited the polaritons as emitters, using respectively their very short lifetime and their very light mass to access a faster cooling dynamics and an energy range going from 150K to 4K.

By studying the interactions of the phonons with a coherent gas of polaritons we have been able to determine the thermal fluxes exchanged between the phonons and the polariton gas. Using those interactions, a novel full optical mean to cool down a microcavity in the strong coupling regime based on polariton ASF has been developed. The characteristics of this cooling methods have been investigated allowing to characterize the mechanisms involved. The relative thermal fluxes associated to each of those mechanisms have been extracted. As an output, we were able to demonstrate that in peculiar conditions, the driven dissipative gas of polaritons act as an out of equilibrium coolant for the lattice.

Chapter 1

Determination of the spatial coherence of a ZnO microwire quantum degenerate one dimensional gas of polaritons

The spatial coherence of a quantum gas of bosons is in principle affected by the dimensionality of the spatial environment and the interactions [15]. This chapter presents the study performed on ZnO microwires polaritons condensate and demonstrates that despite the one dimensional character of those polaritons and despite their quasi excitonic nature, ZnO microwires polariton condensates are featuring spatial coherence on a range of the order of magnitude of that usually reported for two dimensional polaritons. It demonstrates that the condensate is in the vanishing interactions regime and that the correlations are governed by both of the out of equilibrium character of the system and the disorder.

After a motivation paragraph, the state of the art of polariton physics in ZnO will be presented : a short review of the strong coupling regime in ZnO microcavities will be given. The structural properties of the microwires and their growth process will be introduced. The photonic properties of microwires giving rise to intrinsic one-dimensional polaritons will be detailed. The key points of the quantum degenerate regime will be addressed and in particular the influence of the polariton mass. The measurements of the spatial correlations performed on the one dimensional condensate and their interpretation will be presented.

1.1 motivations

The prediction of Bose Einstein Condensation (BEC) was due to Bose [7] and Einstein [8] respectively in 1924 and 1925, the demonstration of a related phenomenon consisting in the observation of the λ point in He was discovered by London in 1938 [16]. Over the last four decades, both cold atoms and solid-state composite bosons communities worked hard to reach the quantum degenerate state. The first achievement of a Bose-Einstein condensate of rubidium atoms was performed by the teams of Cornell, Wiemann [5], and Ketterle [6] in 1995.

Reduced dimensionality quantum degenerate Bose gases were theoretically predicted to display very rich physics like Tonks Girardeau gases in which, in the limit of infinite interactions, bosons trapped in a one dimensional potential become impenetrable and mimics the Pauli exclusion principle [17, 18], and like quasi-condensation, which corresponds to an intermediate interactions regime where phase and density correlations display non-trivial properties. The interested reader could find an extensive review on the low dimensionality quantum degenerates gases in ref [15]. Those theoretical descriptions lead experimentalists to address the challenge of the observation of those effects that were obtained in cold atom gases for Tonks Girardeau gases [19] and quasi condensation regime [20].

Excitons polaritons are the results of the strong coupling regime between the light and the excitons in semiconductor media. They have an integer spin and their low mass ($\sim 10^{-4} m_e$) represents a very interesting advantage in the context of quantum degenerates Bose gases. Bose Einstein Condensation of exciton-polariton, proposed in 1996 [21] has been demonstrated in 2006 in CdTe microcavity [11].

Despite their driven dissipative and open character, degenerates polaritons are featuring the characteristics of weakly interacting Bose gases and have been shown to display the related phenomenology like superfluidity [22], the existence of integer [23] and half integer [24] vortices, as well as bright [25] and dark [26] solitons.

In the low dimensionality context, the first observation of one dimensional polariton condensation was due to the group of Jacqueline Bloch at the Laboratoire de Photonique et de Nanostructures (LPN). One dimensional microstructures were etched in GaAs planar microcavities [27] in order to study more intensively the interactions in a one dimensional quantum degenerate Bose gas of polaritons and its propagation characteristics. Following studies performed in 2D microcavities [28, 29], in ref. [30],the authors demonstrated that

the potential induced by the interaction between the reservoir and the one dimensional condensate was able to generate propagation of the polariton condensate. Then a study of the effect of a weak disorder on the condensate propagation was published by the same team [31]. Those results coupled to theoretical ones [32] obtained on this topic lead to a good understanding of the physical processes involved in the quantum degeneracy of one dimensional polariton gases and especially the key role of the interactions between the polaritons and the excitons of the reservoir. In parallel, the demonstration of the coherence of a 1D polariton quantum degenerate Bose gas was performed on a one dimensional valley of potential within a 2D CdTe planar cavity [33] by the group of Benoit Deveaud at EPFL. Later on the same group demonstrated that the studied quantum degenerate polariton gas was fulfilling the Penrose-Onsager criterion [34] : The authors reconstructed the full single particle density matrix for a one-dimensional polariton condensate, determined its eigenstates and could prove the macroscopic occupation of a single state of the one dimensional polariton nonequilibrium BEC. Following those works, during the last two years, theoretical results dealing with 1D degenerates Bose gases of polaritons and addressing the effect of the phase fluctuations [35] and the ones of the weak interactions [36] on the long range coherence properties of 1D polariton condensates have been obtained.

The ZnO microwire polaritons we have been studying during that PhD have very peculiar characteristics in the context of 1D polariton degenerate gas : It has been demonstrated that those polaritons are intrinsically one dimensional and stable at room temperature [37] and that at T=40K, the polariton lasing mode in those wires exhibits an excitonic ratio as high as 97%. Moreover, thanks to the very high binding energy of the exciton in ZnO (12 times larger than the one of GaAs), the excitonic Bohr radius is as small as 1.8nm (to be compared with the 10nm for GaAs) which results in a lower polariton-polariton interactions in comparison with GaAs.

The first of the motivations of this experimental work was to determine the influence of such a high excitonic fraction on the extension of the spatial coherence of the 1D degenerate Bose gas of polaritons.
In ZnO the value of the diffusion length of the bare exciton is around $200nm$ at 4K [38] , this work demonstrates that the 3% photonic fraction of this polariton gas is large enough to dress the excitonic field allowing it to enter the quantum degeneracy regime at T=40K. We demonstrate that this dressed state features a coherence length of $10\mu m$ which is of the order of magnitude of the coherence length observe in 50% excitonic polariton gases

in planar microcavities [11]. More strikingly which is of the same order of magnitude than the results obtained so far with indirect excitons at much lower temperature [12].

The second purpose of that work was to study the shape of the spatial correlation function of the 1D degenerate Bose gas of polaritons in order to determine how it is affected by the low dimensionality, the very high excitonic ratio, the losses and the low interaction strength. To do so, we performed a quantitative simulation, in collaboration with our colleagues of the Laboratoire de Physique et de Modélisation des Milieux Condensés. A theoretical study based on a driven dissipatitive mean field model developed in the ref. [32] has been developed. It captures the main features of the experimental data and allows to understand that the interactions have a negligible effect on the coherence length of the condensate and that the shallow disorder experienced by the condensate plus the time integrated conditions of the experience are causing the decay of the correlations.

1.2 state of the art on strong coupling regime in ZnO microstructures

1.2.1 Short review of strong coupling regime in ZnO-based microcavities

After having been widely spectroscopicaly studied as a wide bandgap semiconductor material during the 60s (references [39] and [40] provide an extensive review in this context), ZnO was recently rediscovered as a particularly well suited excitonic medium in the context of the strong coupling regime between light and excitons [41]. The large value of the bulk Rabi splitting (300meV to be compared to the 7.8meV of GaAs [10]), the small excitonic Bohr radius and the large binding energy (60meV to be compared with the 4.8meV of bulk GaAs) making it a well suited candidate for high temperature studies of quantum degenerates Bose gases of polaritons.

The first demonstration of strong coupling regime using ZnO as polaritonic medium was reported in a planar microcavity in 2008 by Shimada *et al.* [42]. Another report of ZnO MC strong coupling regime was published by Chen *et al* [43]in 2009. Another contribution to the ZnO polariton community was published in 2009 by Médard *et al.* [44] showing unambiguously strong coupling regime into the investigated MC.

It has been shown that high quality factor microwires are in the strong coupling regime by the team of Prof. Zanghai Chen (Fudan university) [45]).In parallel, we have demonstrated in this system the 1D character of Hexagonal Whispering Gallery Modes (HWGM) polaritons [37] showing also that thanks to the very large Rabi splitting, the polariton gas is preserved from LO phonons broadening even at room temperature.

1.2.2 Quantum degenerates Bose gases in ZnO structures

The topic of exciton quantum degeneracy was introduced in 1962 by Blatt and Moskalenko who independently predicted the Bose Einstein condensation (BEC) of excitons [46, 47]. The idea was that thanks to their very light mass as compared to cold atoms, those composite bosons would be ideal candidates for BEC. After several claims of hints of quantum degeneracy even in the 70s [48, 49], in 2012 hint of spatial coherence in an exciton gas was reported [12]. The authors used indirect excitons in very high quality coupled quantum wells to reach quantum degeneracy at temperature of the order of one tenth of a Kelvin.

ZnO was proposed as a good candidate for room temperature polariton lasing by M. Zamfirescu et al [41], the authors are arguing that the large oscillator strength, the large exciton binding energy and the large Mott density of ZnO are making it the most suited material for room temperature polariton lasing. The first observation of polariton lasing in a ZnO planar cavity [50] was demonstrated by Guillet *et al.* at $T \leq 120K$.

1.3 Introduction to the strong coupling regime in ZnO microwires

In ZnO microwires the light is confined within the microwire cross section by total internal reflection on the facets. As a result the confined photons are strongly coupled to the bulk excitons of the wires which gives rise to polariton modes exhibiting a Rabi splitting equal or close to that of the bulk. This part presents a short introduction of the excitons and of the strong light-exciton coupling regime that gives rise to the polaritons.

1.3.1 Short introduction to the strong coupling regime in semiconductors

ZnO and ZnSe used in the following chapter are direct bandgap semiconductors which means that the minimum of energy of the conduction band and the maximum of the valence band occur at $k = 0$, (the Γ point of the Brillouin zone) cf. e.g. the book of Charles Kittel [51].

When such a semiconductor is submitted to an excitation of energy $E > E_{gap}$ an electron of the valence band can be promoted in the conduction band leaving a hole behind it. The hole behaves as a positively charged particle with a charge $+e$ and an effective mass m_h. See e.g. chapter 8.1 and 8.5 of [39].

Then, owing to Coulomb interaction, electron and hole bind together to form an exciton [52, 53].

During that work, we will only concentrate on excitons with small momenta $\hbar k$ comparable to that of the photons in the medium, which will limit us to a very narrow range of the band structure centered around Γ. In such a limit, both dispersions respectively of the electron and the hole can be approximated by parabola :

$$E_v(k) = E_v(k=0) + \frac{\hbar^2 k^2}{2m_v*} \qquad E_c(k) = E_c(k=0) + \frac{\hbar^2 k^2}{2m_c*} \tag{1.1}$$

With $E_v(k=0)$ resp $E_c(k=0)$ the energies of the electrons in the valence and conduction bands at zero momentum and m_v^* and m_c^* the effective masses of the electrons in those bands (in the case of ZnO, those masses have been mesured to be $0.24m_0$, m_0 being the free electron mass. [54] for the mass of the electron, the mass of the heavy hole being $0.59m_0$ [55] .

It defines the semiconductor bandgap:

$$E_{gap} = E_c(k=0) - E_v(k=0) \tag{1.2}$$

By adding the Coulomb interaction one can find the energy of the exciton using a hydrogen atom like model with effective constants :

$$E_X(n, K) = E_g - Ry^* \frac{1}{n^2} + \frac{\hbar^2 K^2}{2M} \tag{1.3}$$

With: n the principal quantum number of the hydrogenoïd system, $Ry^* = 13.6eV\frac{\mu}{m_0}\frac{1}{\epsilon^2}$ (m_0 being the free electron mass) the effective Rydberg energy [56] which is called binding energy of the exciton.$M = m_e + m_h$ the translational mass of the exciton. ϵ being defined as $\epsilon = \epsilon_0 \times \epsilon_r$ With ϵ_0 the electric permittivity of free space and ϵ_r the relative permittivity, and K its center of mass wavevector. μ is the reduced mass of the exciton written as:

$$\mu = \frac{m_e m_h}{m_e + m_h} \tag{1.4}$$

And a_B the excitonic Bohr radius defined by:

$$a_B = a_B^h \epsilon \frac{m_0}{\mu} \tag{1.5}$$

With a_B^h the Bohr radius of Hydrogen.

The effective Rydberg energy and the Bohr radius are respectively $Ry^*_{ZnO} = 60meV$ and $a_{B(ZnO)}1.8nm$ for ZnO and $Ry^*_{ZnSe} = 19.9meV$ and $a_{B(ZnSe)} = 4.5nm$ for ZnSe those values have to be compared with $Ry^*_{GaAs} = 4.2meV$ and $a_{B(GaAs)} = 15nm$ for GaAs. We will see later that a high binding energy and small Bohr radius play a crucial role in our study.

The limits of the exciton as a boson Excitons are composite bosons, made up of two fermions. They behaves as bosons when the exciton density is low enough. When the density becomes too large (a naive picture would describe it as larger than one exciton per a_b^3) the Pauli blocking starts to unbind excitons that are loosing their bosonic nature. This density is called the Mott density correspond to the phase transition between the exciton gas and the electron-hole plasma. A derivation of the Mott density can be found in the chapter 21 of ref. [39].

According to this reference the Mott density for bulk ZnO is :

$$n_M^{ZnO} \approx 4.5 \cdot 10^{17} cm^{-3} \tag{1.6}$$

Which corresponds to a mean interparticles distance or the order of $8a_b$. This value has to be compared with the polariton correlation function determined in 1.4.5 .

Bulk polaritons as eigenstates of a bulk semiconductor In 1958, J.J. Hopfield [57] made a semiclassical description of the coupling of a $3D$ exciton to the light. He demonstrated that in an infinite 3D crystal the interaction between the excitonic polarization field and the propagating electromagnetic field are in the strong coupling regime.

The derivation of those states by C.L. Andreani can be found e.g. in the chapter two of the book [58].

A simple model to describe the strong coupling regime in planar semiconductor microcavity. Let us consider a photon confining microstructure featuring an infinite quality factor in which photons are interacting with an excitonic medium. The lifetime of the photon and the decoherence time of the exciton are infinite.

The momentum of the photons is quantized by the confinement and will be quoted $k_\perp$ for the quantized component and $k_\parallel$ in the directions in which the momentum is not confined.

If the photon mode energy is well described by a harmonic oscillator at $k_\parallel$ momentum and the excitonic one as well at the same momentum, and if we take in account the coupling strength between those two modes $V_0 = \frac{\hbar\Omega_R}{2}$, we can write the Hamiltonian of the coupled oscillators as :

$$H = \begin{pmatrix} E_x(k_\parallel) & V_0 \\ V_0 & E_{ph}(k_\parallel) \end{pmatrix} \tag{1.7}$$

The value of the coupling Ω_R is connected to the oscillator strength as : $\Omega_R \propto \sqrt{f}$, with f the oscillator strength of the considered exciton.

The eigen energies of this hamiltonian are :

$$E_{lp}(k_\parallel) = \frac{1}{2}[(E_{ph}(k_\parallel) + E_{ex}(k_\parallel)] - \frac{\hbar}{2}\sqrt{\delta^2 + \Omega_R^2} \tag{1.8}$$

$$E_{up}(k_\parallel) = \frac{1}{2}[(E_{ph}(k_\parallel) + E_{ex}(k_\parallel)] + \frac{\hbar}{2}\sqrt{\delta^2 + \Omega_R^2} \tag{1.9}$$

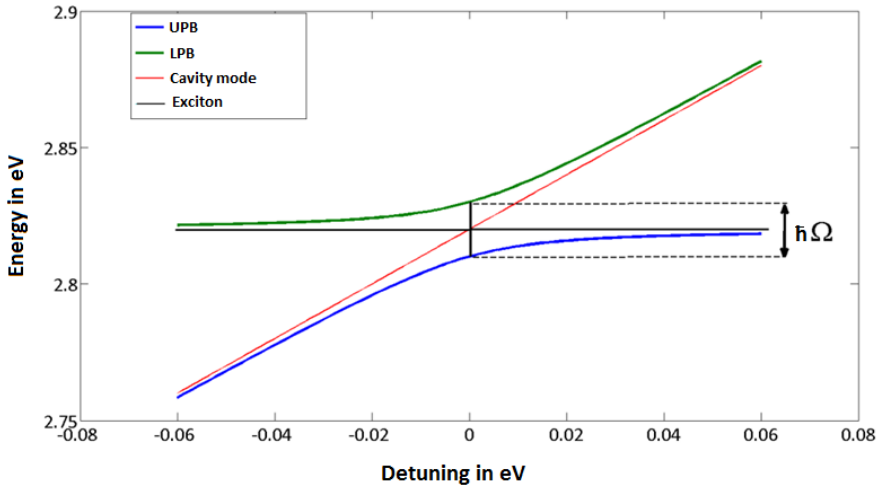

Figure 1.1: Upper and lower polariton branches energies versus detuning (the parameters are the ones of the ZnSe planar cavity investigated in the chapter 2)

Where $\delta(k_\parallel)$, the photon/exciton detuning is defined as:

$$E_{ph}(k_\parallel) - E_{ex}(k_\parallel) = \hbar\delta(k_\parallel) \tag{1.10}$$

Those two states are called upper and lower polaritons. Their exciton/photon ratio are X_k and C_k respectively.

$$X_k^2 = \frac{\delta_k + \sqrt{\delta_k^2 + \Omega_r^2}}{2\sqrt{\delta_k^2 + \Omega_R^2}} \tag{1.11}$$

$$C_k^2 = 1 - X^2 \tag{1.12}$$

C_k^2 and X_k^2 are called the Hoppfield coefficients, they represent the photonic and the excitonic fractions in the polariton field.

At $\delta_k = 0$, one has C_k^2=X_k^2=1/2 and $E_{up} - E_{lp} = \hbar\Omega_R$. This is the conditions around which the anticrossing behavior which is the characteristic of the strong coupling regime takes place cf. Fig. 1.1

To derive a more realistic model, one has to take in account the losses of the cavity limiting the lifetime of the photons and the dephasing time accounting for non radiative losses of the exciton. To do so one can add a relaxation coefficient to the photon/exciton

energies as:

$$E^*_{ph}(k_\parallel) = E_{ph} - i\hbar\gamma_{ph} \tag{1.13}$$

$$E^*_{ex}(k_\parallel) = E_{ex} - i\hbar\gamma_{ex} \tag{1.14}$$

Substituting those values in 1.9 and 1.8 allows to determine a more realistic condition on Ω_R, γ_{ph} and γ_{ex} to enter the strong coupling regime and which could be written as :

$$\Omega_R > \gamma_{ph} \qquad \text{and} \qquad \Omega_R > \gamma_{ex} \tag{1.15}$$

In our case, the Rabi splitting of the investigated structures is of the order of $300meV$, using non linear spectroscopy investigation the linewidth of the exciton is found to be $200\mu eV$ at 40K in [59] and to be $550\mu eV$ in [60] and the photonic linewidth has been calculated to be of the order of $1meV - 4meV$ [61]. This criterion is fulfilled within several orders of magnitude by the investigated structures.

1.3.2 Zinc Oxide : a large bandgap semiconductor

ZnO is a wide bandgap II/VI semiconductor (oxygen is a VI element and Zinc a II), which is of wurtzite crystalline structure (cf. Fig. 1.2). This structure is at the origin of the hexagonal shape of the ZnO microwires studied during that work. This part describes its structural and optical properties which are necessary to a good understanding of polaritons in ZnO. The end of that section is devoted to a comparison with the other semiconductor materials employed in polariton physics.

Bulk Zinc Oxide optical properties Zinc Oxide features a direct bandgap of 3.37eV at room temperature. It exhibits strongly ionic bonding $Zn^{2+} - O^{2-}$. The most interesting aspects of ZnO from the point of view of the polariton physic are the following :

- (i)The large binding energy of the exciton ($60meV$) which is 2.4 times larger than the thermal energy at RT [62].
- (ii)The large oscillator strength ($f \sim 40000meV^2$) [40].
- (iii)The small Bohr radius of the exciton ($1.8nm$)[63].

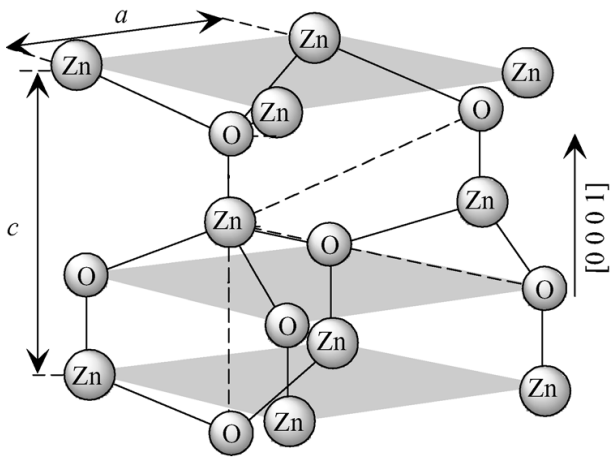

Figure 1.2: Schematic representation of a wurtzitic ZnO structure with lattice constants a in the basal plane and c in the basal direction, taken from [55]

- (iv) The large Mott density $4.5 \times 10^{17} cm^{-3}$ [62]

There is another important parameter of ZnO that plays a key role in this work :

- The energy of the LO phonon in ZnO is $72meV$. This value is significantly smaller than the Rabi. As we have shown it in a previous work, this feature prevents LO phonon induced decoherence of the polariton by preventing the scattering toward the exciton states [37].

Among the twelve possible exciton states in ZnO the exciton-photon selection rules puts forward three major bright levels. Because of degeneracy two of them : $A\Gamma_5$ and $B\Gamma_5$ are twice degenerated and are coupled with $E \perp C$ light and $C\Gamma_1$ coupled to $E \parallel C$ light (the table 1.1 summarize their characteristics).

Comparison of the optical ZnO characteristics with the ones of the other usual semiconductor materials employed in strong coupling microstructures The table 1.2 allows to compare the Bandgap, Bohr radii, binding energies, oscillator strength and the Mott density of GaAs which was the most studied semiconductor in the context of strong coupling, CdTe the II/VI semiconductor in which BEC was demonstrated [11] followed by the studies of 1D condensate trapped in a disorder valley [33] [34]. It also gives those parameter for GaN which, like ZnO is a good candidate for quantum degeneracy at room temperature. Finally, those parameters are also given for ZnSe, the semiconductor material employed in the planar cavity studied in the second chapter of that manuscript.

Exciton	Energy at 0K (meV)	Energy at 300K (meV)	LT splitting (meV)	oscillator strength (meV^2)	Polarization selection rules
A	3375.5 [64]	3309 [40]	1.5 [40]	10000 [62] 15000 ± 5000 [60]	E$\perp$ C
B	3381.5 [64]	3315 [40]	11.1 [40]	73600 [62] 250000 ± 5000 [60]	E$\perp$ C
C	3420 [64]	3355 [40]	13.9 [40]	93300 [62]	E $\parallel$ C

Table 1.1: Characteristics of the excitons in ZnO.

Material	Bandgap	Bohr radius	Binding energy in bulk(quantum wells)	Oscillator strength	Mott density in bulk (quantum wells)
GaAs	1.43eV [65]	112Å[65]	4.8 ($\sim$14) meV [65] ([66]	$\sim$250 meV2 [10]	$3 - 12 \times 10^{16} cm^{-3}$ ($\sim 4 \times 10^{10} cm^{-2}$) [67]
CdTe	1.43eV[65]	70Å[65]	10 ($\sim$25) meV [65],[68]	$\sim 1000 meV^2$ [68]	$0.5 - 2 \times 10^{18} cm^{-3}$ ($\sim 1 \times 10^{12} cm^{-2}$) [69]
3*				X_A $0000 \pm 5000 meV^2$	$2 - 3 \times 10^{18} cm^{-3}$
GaN	3.44eV [65]	24Å[65]	26 ($\sim$50) meV [70] [71]	X_B $9000 \pm 5000 meV^2$ [60]	($\sim 2 \times 10^{12} cm^{-2}$) [146]
				X_C $000 \pm 1500 meV^2$	
ZnO	3.437eV [39]	18Å[62]	60 meV [62]	$\sim 10000 meV^2$ (A exciton)[62]	$0.5 - 20 \times 10^{18} cm^{-3}$ [62]
ZnSe	2.7eV [65]	45Å[65]	17meV[72]		

Table 1.2: Comparison of the key characteristics of the excitons in usual polaritonic media.

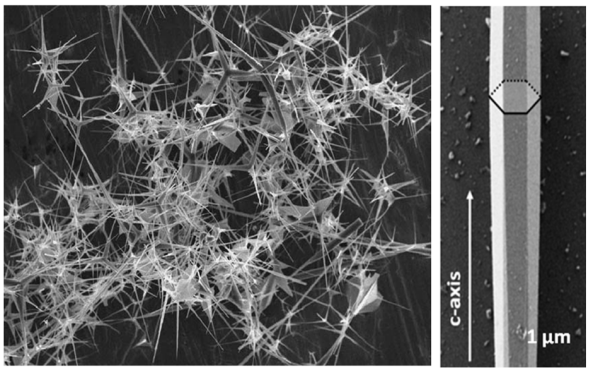

Figure 1.3: Left panel : as grown ZnO Tetrapods, Right panel : single ZnO microwire

1.3.3 ZnO microwires structural properties and growth process

Our microwires are fabricated by the team of prof. Zhanghai Chen of Fudan university. The technic used is vapor phase transport. It consists in submitting high purity Zinc Oxide powder to high temperature (900°) at room pressure. The experimental apparatus contains a cooled substrate on which zinc oxide tetrapods are growing spontaneously cf. left panel of Fig.1.3 .

Each of the four ZnO microwires composing a tetrapod is a ZnO single crystalline structure with the C Axis parallel to the wire axis.

For our optical experiment, the tetrapods are mechanically broken into single wires cf. right panel of Fig.1.3 those wires are then deposited and aligned on a sapphire substrate using X,Y,Z translation stages equipped with a micro probe tip.

The crystalline quality of the microwires is found to be excellent, with an inhomogeneous excitonic linewidth as low as $1.8meV$ at 4K.

1.3.4 Optical properties of ZnO microwires

In the ZnO microwires studied during that work, the light is confined inside the wire thanks to the total internal reflection on the facets. owing to this mechanism, we labeled those modes Hexagonal Whispering Gallery Modes (HWGM). This part briefly introduces the spatial confinement of the light in the wire and presents the key physical parameters that will be used afterwards.

Hexagonal whispering gallery modes in the wire cross section Here the key results of the light confinement in the wire cross section are presented. The reader can find an extensive description of these modes in ref.[73]

Using a geometrical approximation, assuming that the length of the beam-path along one roundtrip must be equal to an integer number of wavelength. By taking in account the phase added at each reflection, we end up with the following equation taken from [74] which determines the wavelength $\lambda_{m,TE/TM}$ of the HWGM.

$$6R = \frac{\lambda_{m,TE/TM}}{n_0}\left(m + \frac{6}{\pi}\arctan\left[\beta_{TE/TM}\sqrt{3n^2-4}\right]\right) \tag{1.16}$$

Where R is the radius of the wire, n_0 the background index, m the azimuthal number, β accounts for the TE/TM polarization splitting $\beta_{TE} = n^{-1}$ and $\beta_{TM} = n$.

This description is valid when $\lambda \to 0$ (which means $m \gg 1$)

Our typical ZnO microwire have a diameter of $1\mu m$, with a wavelength in the vicinity of the exciton of $375nm$, and a background index $n = 2.6$. We end with an azimuthal number $m \approx 18$ this shows that this raylight model is acceptable in our case and constitute a first good approach to determine e.g.the free spectral range.

A more accurate and realistic method to describe the photonic confinement within the cross section of the microwire requires a wave model, this theoretical study [61] has been developed by the group of Guillaume Malpuech in the Blaise Pascal university of Clermont Ferrand.

Photonic relation of dispersion In a microwire, the photons are confined in the x,y plane and free to propagate along the z axis.

Their k_x, k_y momenta are quantized and only k_z is a "good quantum number".

The relation of dispersion of light in the wire reads :

$$E(k_z) = \sqrt{E^2(k_z = 0) + \left(\frac{\hbar c k_z}{n}\right)^2} \tag{1.17}$$

For small k_z, such that $\frac{\hbar c k_z}{n} \ll E_0$:

$$E(k_z) = \sqrt{E_0^2 + \left(\frac{\hbar c k_z}{n}\right)^2} \approx E_0 + \frac{(\hbar k_z)^2}{2M^*} \tag{1.18}$$

Where M^* is the effective mass of the photonic mode that reads:

$$M^* = \frac{n_0^2 E_0}{c^2} \tag{1.19}$$

n_0 being the refractive index of the medium.

In our case this effective mass is of the order of $10^{-5} m_0$ in the range of energies we are interested in.

Peculiarities of the strong coupling regime in ZnO microwires

As described previously, thanks to their waveguiding shape, ZnO microwires studied during that work are intrinsic photon confining structures. An interesting aspect of those wires is that since the photons are confined inside the wire, their wavefunction is strongly localized inside of it. The confined photons are permanently interacting with the excitonic medium : this makes the ZnO microwires intrinsic strong coupling microstructures. This part presents the key aspects of the strong coupling regime in the ZnO microwires.

Rabi splitting of the wire During that work only A and B excitons were excited using a fully polarized laser with $E \perp$ to the C axis.

Since the energy difference between those two levels (6meV) is much smaller than their corresponding bulk Rabi splitting (respectively $135meV$ for the A exciton and $268meV$ for the B one), their oscillator strengths can be meaningfully merged into a single one allowing to obtain a total bulk Rabi splitting : $\Omega_{bulk,E\perp C} = \sqrt{\Omega_A^2 + \Omega_B^2} = \sqrt{(135meV^2 + 268meV^2)} = 300meV$.

Exciton-photon overlap in the wire A large volumic fraction of the photonic mode interacts with the excitonic medium during its lifetime in the cavity which leads to a photon-exciton overlap close to unity.

By expressing the effective Rabi splitting of the wire Ω_{wire} for a given photonic mode γ as a function of the bulk Rabi splitting (Ω_{bulk}) and the exciton-photon overlap integral α one gets :

$$\Omega_{wire} = \alpha\Omega_{bulk} \tag{1.20}$$

Where $\alpha = || \int_x \int_y \int_z \Psi_X^*(x,y,z)\Psi_\gamma(x,y,z)dxdydz||^2$

Ψ_X and Ψ_γ being respectively the excitonic/photonic wavefunctions.

In our case, the Rabi splitting of the wire has been mesured at $288meV \pm 29meV$ which allows to estimate :

$0.93 \leq \alpha \leq 1$

Microwire : a multi-mode polaritonic system The wavelength quantization condition 1.16 induce an energy difference between two consecutive HWGM which reads :

$$\Delta\lambda =| \lambda_m - \lambda_{m+1} | \ll \frac{\Omega_R n_0}{2\pi c} \Leftrightarrow \Delta E =| E_m - E_{m+1|} | \ll \Omega_R \tag{1.21}$$

Several photonic modes are fulfilling this condition and thus are coexisting in the wire, having theoretically orthogonal wavefunctions. This implies that the exciton wavefunctions involved in one polariton states are different of the ones involved in one other, thus the oscillator strength to be taken in account is the entire one of the bulk instead of being distributed on the different polariton states.

We end with a set of n 2×2 matrix each one of them coupling the n^{th} photonic mode to the bulk exciton giving rise to the n^{th} polariton state in the wire instead of having a n one with the oscillator strength of the excitons distributed between the n polariton states.

In this way each one of the polariton state of the wire features in principle the same Rabi splitting $\Omega_{wire} = 288meV \pm 29meV$

This multimode of the microwire polaritons is shown on the Fig. 1.12.

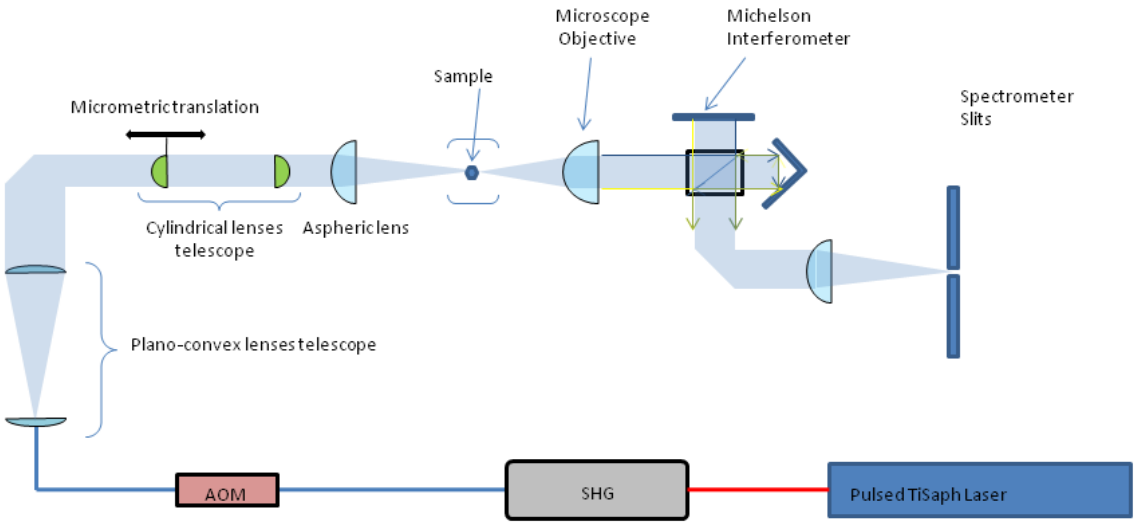

Figure 1.4: Scheme of the experimental setup.

Using this full set of polariton branches and fitting the dispersions with a single set of parametters (Rabi energy, background index, excitonic energy) and using only the energies of the photonic modes as free parametters allows to precisely determine the Rabi splitting in the wire. [75].

1.4 One dimensional Zinc Oxide Polariton spectroscopy

This section describes the experimental way used to access the spectroscopic data discussed in this work. The scheme of the setup is presented on the figure 1.4.

1.4.1 Non-resonant injection

The photoluminescence experiments presented in this chapter were realized under non resonant excitation meaning that the laser energy was tuned to the energy of the A-B excitons bands (cf. Fig. 1.5). The laser thus generates free excitons. Then, owing to exciton-phonon and exciton-exciton scattering, excitons relax from this excitonic reservoir to the polariton states.

This excitation method offers several advantages :

- Thanks to the mirror-less structure of ZnO microwires, there is no need to pump through the sideband minima of a Bragg plateau which enhance the efficiency of the pumping and the exciton reservoir can be pumped directly.
- Thanks to the very high absorption coefficient of ZnO at this energy ($\sim 10^5 cm^{-1}$), it allows to populate efficiently the free exciton levels . In opposition with an excitation far above the bandgap, it limits heating effects of the excitons and the phonon bath and simplifies the dynamics.
- The relaxation process scattering the exciton from the reservoir to the polariton state washes the laser coherence guarantying that the measured coherence comes from the polariton condensate and is really spontaneous.

Excitation setup The pico second TiSaph laser provides high peak power allowing to inject instantaneously a large density of free excitons and therefore to reach the critical density of polaritons which allows to cross the polariton laser threshold without being too much disturbed by the absorption related heating effects which are related to the average power. The laser frequency is doubled from NIR to NUV which provides wavelength matching A/B excitonic transitions in ZnO.

The injection part of the setup is successively composed by an acousto-optic modulator which is used as a chopper to further prevent heating issues (the commonly used duty cycle is around 1%) the Fig. 1.6 gives a schematic representation of the injection setup.

In order to get a spatially homogeneous excitation, a slightly defocused cylindrical lenses telescope is used to elongate the excitation spot on the injection side (cf. Fig. 1.7), an aspheric lens focalises it onto the wire.

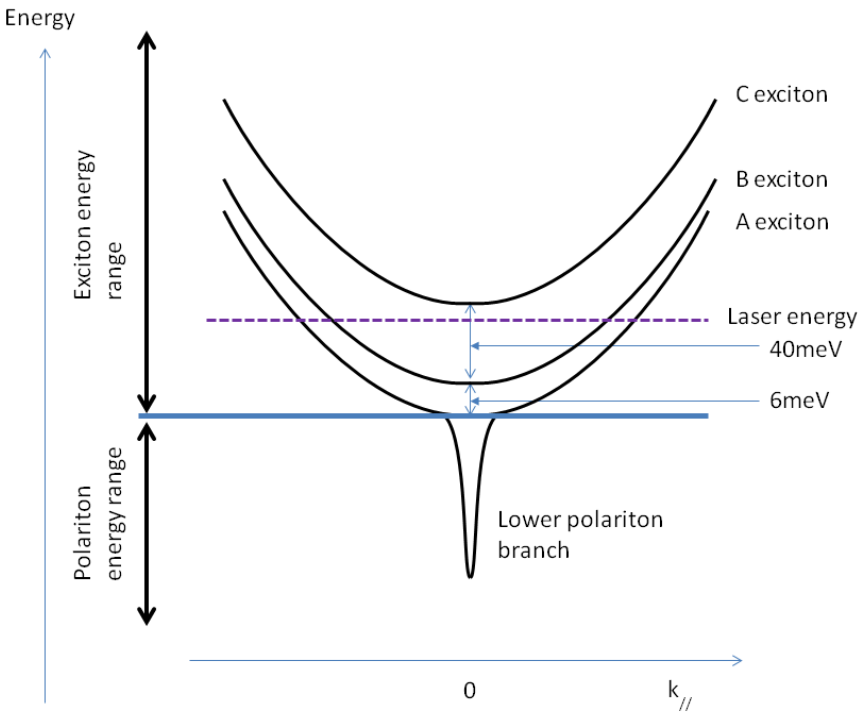

Figure 1.5: Representation of the energy-impulsion relation of the A,B an C excitons and of the polariton states, the energy of the laser correspond to the non resonant injection described in the Polariton non resonant excitation paragraph

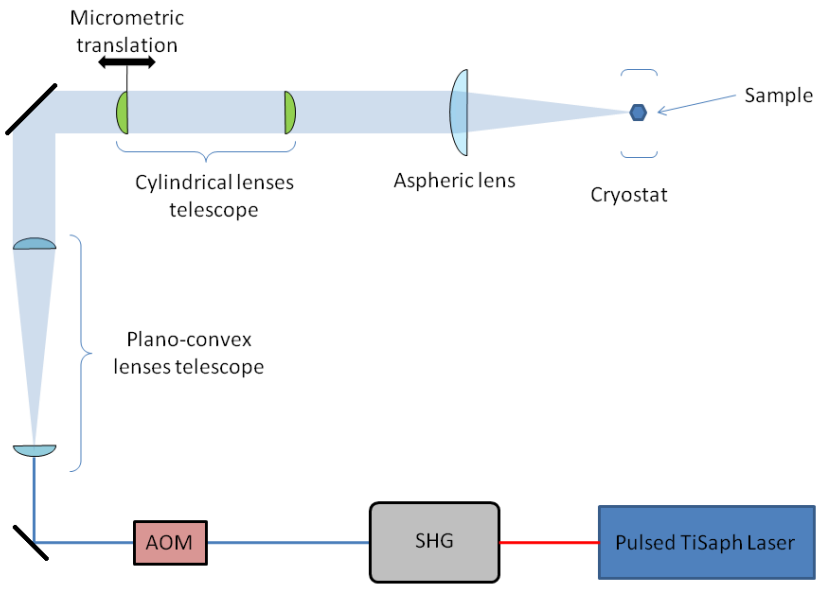

Figure 1.6: Injection part of the setup

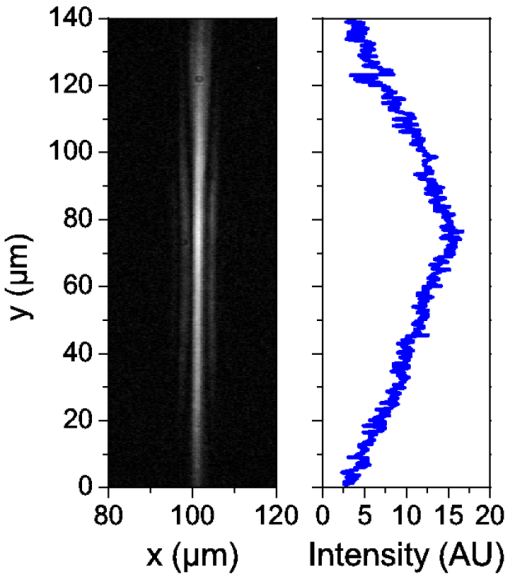

Figure 1.7: Intensity repartition of the excitation spot

1.4.2 Fourier Spectroscopy

Energy-momentum conservation rules When a polariton reaches the surface of the microwire and emits a photon at this interface owing the translational invariance of the system along the z axis, it fulfills the following conditions:

$$E^{in}{}_{Pol} = E^{out}{}_{Photon} \quad \text{and} \quad k_z^{in}{}_{Pol} = k_z^{out}{}_{Photon} \tag{1.22}$$

Where k_z^{in}, k_z^{out} are respectively the components of momenta of the polariton inside the wire and of the photon outside which are parallel to the free axis (cf. left panel of Fig. 1.8), and E^{in}_{Pol} and E^{out}_{Photon} the respective energies of the polariton and of the photon.

Angle resolved space set-up Using an angular and spectraly resolved experiment allows us to measure both of the energies and the angle of emission of the emitted photons.

The energy-momentum relation for a photon in vacuum reads:

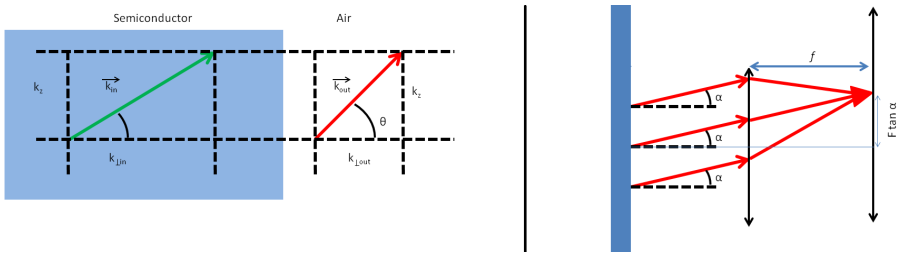

Figure 1.8: Left panel : Representation of the relationship between k_{zin} and k_{zout} respectively the component of the momentum parallel to the c axis of the wire, inside and outside of the wire. Right panel : Schematic representation of the imaging in the Fourier plane

$$E_{photon} = \hbar c k \tag{1.23}$$

By measuring the angle of emission of the photons, we can infer the component of their momentum which is parallel to the interface. thank to the following relation.

$$k_z^{in}{}_{Pol} = \frac{E_{Photon}^{out}}{\hbar c} \sin\theta_{out} \tag{1.24}$$

This last equation links the quantities we can measure (i.e. the angles of emission and the energy of the emitted photon)to the parallel component of momentum of the polariton within the wire and allows us to well define the polaritons dispersion within the wire.

Fourier imaging, energy-momentum detection All the angle resolved experiments performed used Fourier imaging spectroscopy. As shown on the left panel of Fig. 1.8 by imaging the Fourier plane onto the spectrometer slits one can detect both of the energy and of the angle of emission. The objective used during that work features a numerical aperture of 0.5 allowing to perform measurements in a window of angle of emission as large as 60°

By choosing the orientation of the wire parallel or perpendicular to the spectrometer slits, we are able to determine the dispersions along the θ and ϕ angles (right panel of the Fig. 1.9.

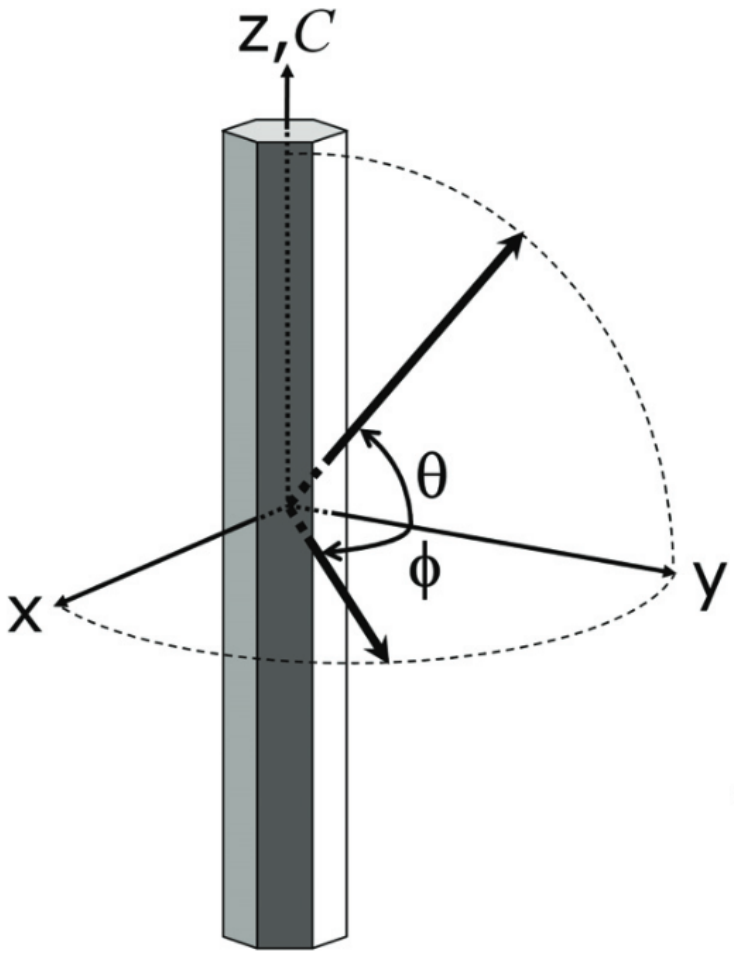

Figure 1.9: Angles of detection along which the dispersions are measured.

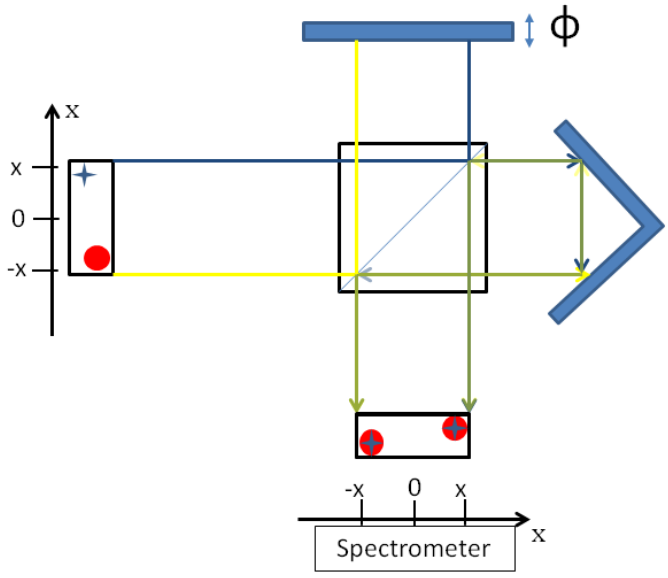

Figure 1.10: Schematic representation of the modified Michelson interferometer used to probe the spatial coherence of the polariton condensate.

The experimental setup used during that work is designed to perform both space and angular resolved spectroscopy experiments by switching one single lens allowing to image alternatively the momentum space or the real space onto the CCD camera.

Modified Michelson interferometer, principle of the spatial first order correlation function measurement Thanks to the linear relationship between the polariton field within the wire and its PL outside, probing the coherence of the light leaking out of the wire allows us to determine the coherence of the polaritons condensate.

The way used to probe that coherence consists in using a modified Michelson interferometer cf. Fig. 1.10 which is equipped with a piezoelectric actuator to sweep the relative phase between the two interferometer arms by a fraction of wavelength. Recording the interference pattern for a full set of phase differences allows to build an interferogram.

One of the interferometer arms is equipped with a reflective retroreflector which performs a centrosymetric transformation of the image. This consists to inverts the the x coordinate with the $-x$ one and the y one with $-y$ on one of the beams. The two beams are carefully overlapped with the autocorrelation point in the middle of the slits of the monochromator. The light emitted by the x point is interfering with the one emitted by the $-x$ one ($x = 0$ being the autocorrelation point which is the point of the wire located on the optical axis).

In order to sweep the relative phase, the piezo actuator is tuned to perform $\lambda/15 \simeq 25nm$ steps starting from the zero delay position. For each step the two interfering images are recorded by the CCD camera at the output of the monochromator. A full measurement sequence consist in 200 frames. The two arms intensities I_1 and I_2 are recorded. The contrast $C(x, -x, \omega, \tau = 0)$ is fitted by a sine function on the interferogram for each one of the pixels of each frame, the residues of the fits are used to evaluate both of the error bars and the validity of the fits. The Fig. 1.11 shows both of the experimental data obtained for the two pixels designed by the blue and red arrows on the left interferogram of the Fig. 1.22 and the sine fit applied to extract the contrast. The wavelength and the position are deduced from the position of the pixel on the CCD chip and from the setup transfer function. This contrast, normalized by both of the arms intensities provides a measurement of the $g^{(1)}(x, -x, \omega, \tau = 0)$ function of the light leaking out of the polariton gas which reads :

$$g^{(1)}(x, -x, \omega, \tau = 0) = C(x, -x, \omega, \tau = 0)/\sqrt{I_1(x, \omega)I_2(-x, \omega)} \tag{1.25}$$

Thanks to the linear relationship between the polariton field inside the wire and the photonic one outside of it, the Eq. 1.25 is equal to the $g^{(1)}(x, -x, \omega, \tau = 0)$ time integrated first order normalized spatial correlation function at zero delay of the condensate which reads :

$$g^{(1)}(x, -x, \omega, \tau = 0) = \frac{\int_T \psi(x,t)\psi^\dagger(-x,t)dt}{\sqrt{\int_T \mid \psi(x,t) \mid^2 dt \int_T \mid \psi(-x,t) \mid^2 dt}} \tag{1.26}$$

Notice the time integrated nature of this expressions which plays a key role in the interpretation of the results.

1.4.3 Linear properties

A previous work performed on those wires [37] demonstrated that in the studied ZnO microwires, the strong coupling regime is achieved. The Rabi splitting is found to be: $\Omega = 288meV \pm 29meV$ at $10K$

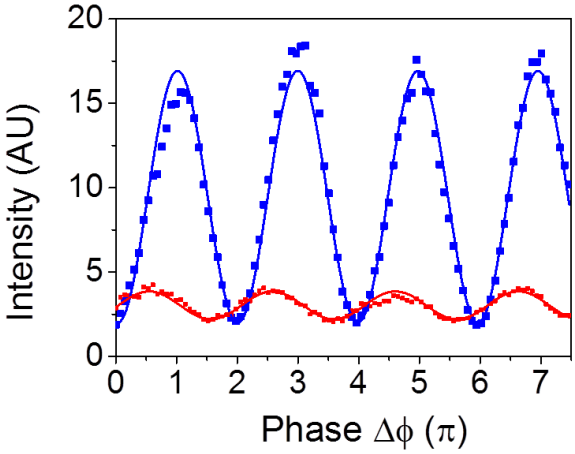

Figure 1.11: Representation of the experimental data of the contrast obtained on two pixels (respectively corresponding to the blue and red arrows on the Fig. 1.22) on a 2λ shift and of the sine fits applied on it. The amplitude of the sine function fitting the data defines $C(x, -x, \omega, \tau = 0)$

The experimental way to acces the Rabi splitting consists in fitting the full set of polaritons branches using

The linewidth of the mode Γ is found to be $\Gamma = 3.1meV \pm 0.2meV$ at $3.22eV$. The figure of merit of the strong coupling regime is thus equal to $\frac{\Omega}{\Gamma} = 93$

One dimensional polaritons The Fourier spectroscopy allows to determine the polariton dispersions along the z axis and perp to that direction.

The upper panel of Fig. 1.13 shows the dispersions along the θ angle (cf.Fig 1.9) which corresponds to polaritons momenta along the axis of the wire.

Because of its hexagonal shape, the wire is invariant by a 60° rotation The lower panel of Fig. 1.13 shows the polariton dispersions along the ϕ angle (cf. Fig. 1.9) in a measurement range of $-30° + 30°$ at $\theta = 0°$ thus this measurement demonstrate that the polaritons are dispersionless, i.e. purely monomode in the plane perpendicular to the wire. This demonstrates the one dimensional character of the polaritons in those ZnO microwires.

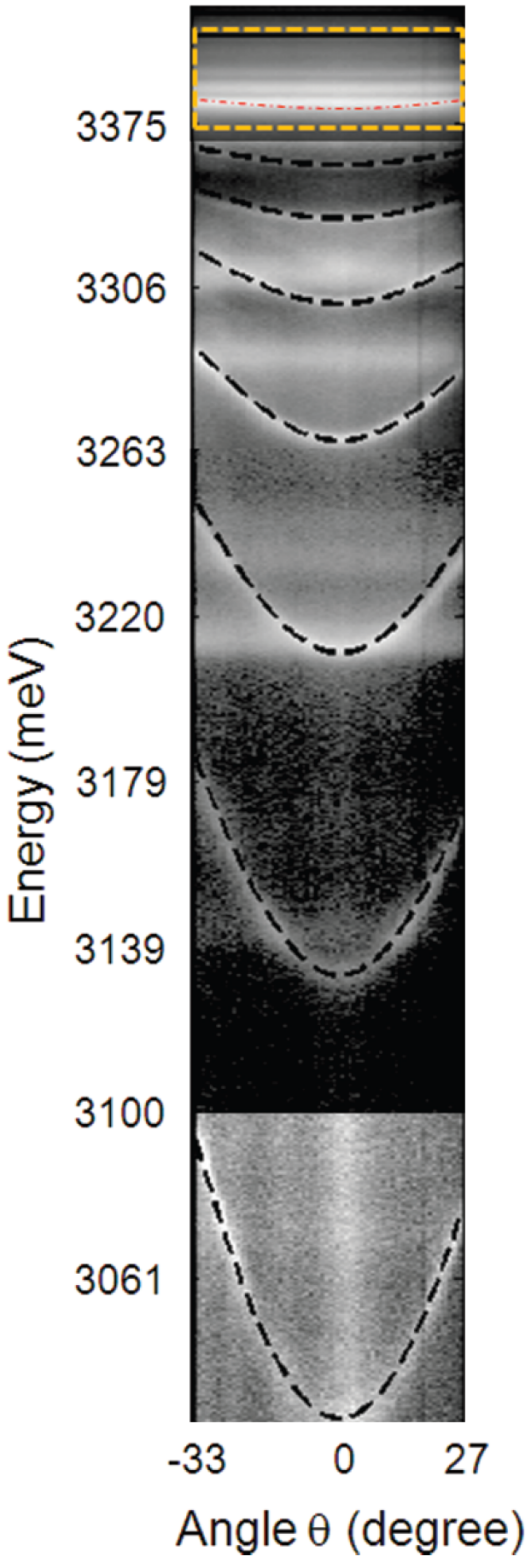

Figure 1.12: Angle resolved photoluminescence data. Set of lower polariton branches. The dashed line yellow rectangle highlight the energetic region of interest in our study

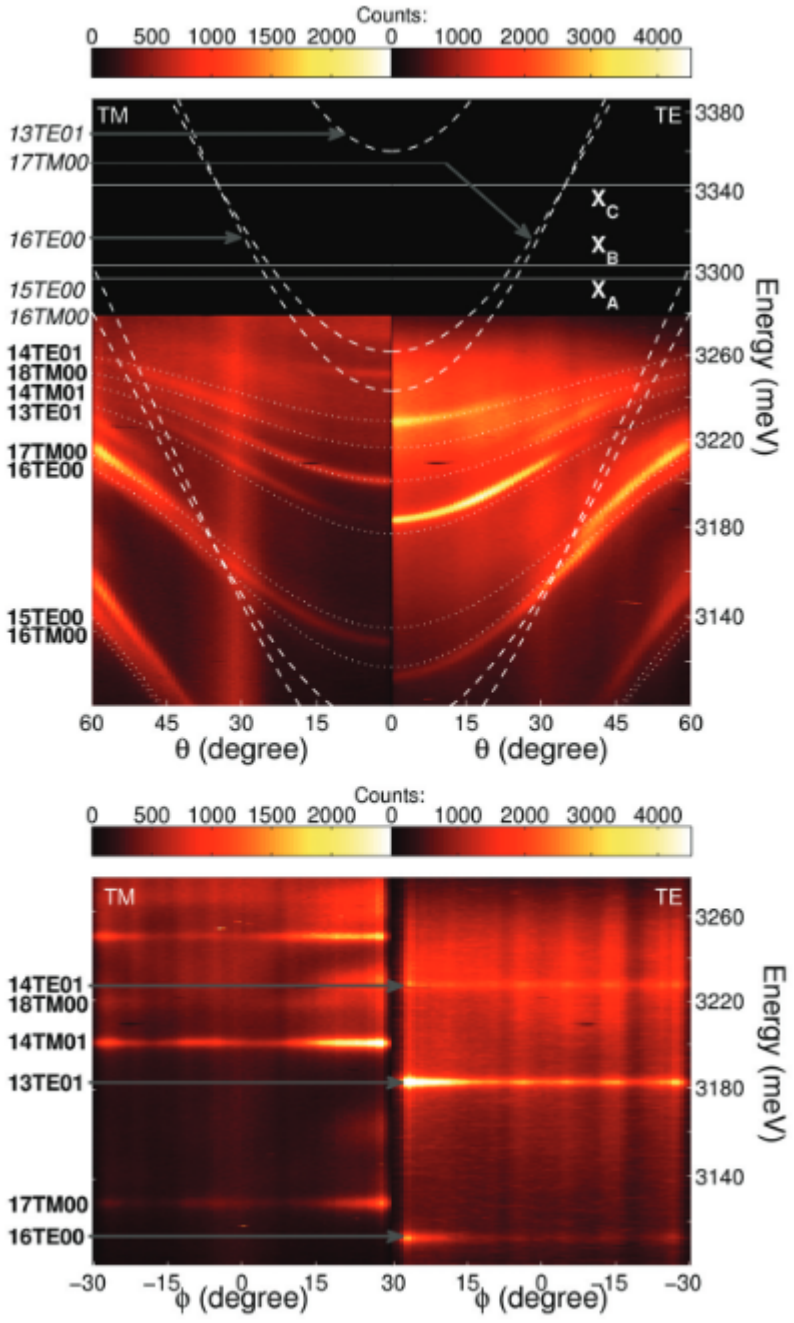

Figure 1.13: Dispersions of the polariton states along Θ (upper panels) and Φ lower one. The left panels are corresponding to a TM polarized detection, the right ones to a TE one.The uncoupled HWGM modes are noted xxTE/TMyy, xx standing for m, the azimuthal quantum number and yy for j, the radial number [37]

Protection of the polariton states against the LO phonon decoherence This work also demonstrated that thank to the very large value of the Rabi splitting in those

wires, the polariton modes, even with a significant excitonic fraction, are protected against thermal phonon decoherence, the phonons being not energetic enough to scatter polaritons to the excitonic reservoir [37].

excitonic fraction determination The Fig. 1.12 shows angle resolved photoluminescence data taken at $40K$, it shows polaritons states that are energetically very close to the excitons as compared to GaAs microcavities polaritons, they are still narrow ans well defined which is unusual in planar microcavities.

The excitonic fraction is determined using the fact that the effective mass m_p of the polariton states depends on the photonic weight $|G|^2$ fulfilling the following relation :

$$\frac{1}{m_p} = \frac{|G|^2}{m_g} + \frac{|X|^2}{m_x} \tag{1.27}$$

With m_g the bare cavity effective mass and m_x the bare exciton mass. $|X|^2$ and $|G|^2$ being respectively the excitonic and photonic fractions of the polariton state.

For the mode we will be interested in the following cf. Fig. 1.14, using the Rabi splitting determined previously i.e. $\Omega = 288meV \pm 29meV$, and using $m_g = n_0\hbar\omega_p/c^2$, $n0 = 2.35$ being the ZnO background dielectric constant of ZnO, one gets :

$|G|^2 = 2.4\%$.

Reasons for the stability of polaritonic states of high excitonic fraction The studied microwires are featuring a Rabi splitting of $\Omega = 288meV \pm 29meV$, the magnitude of the excitonic homogeneous plus inhomogenous broadening has been measured to be as low as $1.8meV$ at cryogenic temperature, the thermal energy is $kT \approx 3meV$. The combination of those parameters avoid the thermal excitation to scatter polaritons into the excitonic reservoir, and despite the very high excitonic fraction and proximity of the excitonic reservoir, the polaritons are remaining stable [37].

1.4.4 ZnO polariton laser properties

This subsection introduces the characteristics of the ZnO 97% polariton lasing state studied during that work. It will address the behavior of this polariton state in terms of

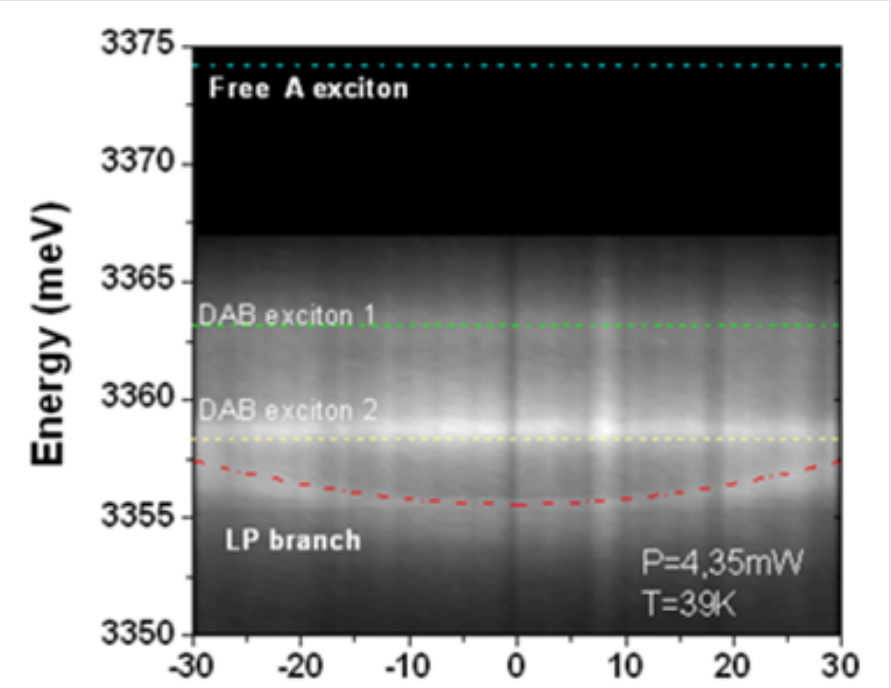

Figure 1.14: Angle resolved photoluminescence spectrum of the 97% excitonic lower polariton branch below threshold and theoretical fit of this branch. The two higlighted Donor-Acceptor excitons The DAB exciton 1 is probably linked to a halogen donnor and DAB exciton 2 to an aluminium donnor [63]

linewidth blueshift and intensity below, across and over threshold in order to demonstrate that the strong coupling is preserved when entering the degeneracy regime.

By increasing the pumping power, a macroscopic population suddenly appears in $k_z = 0$ in a polariton mode $20meV$ below the A exciton. The Fig. 1.14 is a spectral magnification of the Fig. 1.12 on the mode in which appears the macroscopic population. The Fig. 1.15 displays the same spectral region over threshold.

Polariton laser blueshift, linewidth and intensity below, across and above threshold

The figure 1.16 shows the evolution of the blueshift of the polariton state versus the excitation power (normalized at threshold)under non resonant excitation conditions (cf.1.4.1). It demonstrates that the blueshift remains below 1meV with the excitation power up to ten times the power at threshold. This value being compared with the energy difference between the excitonic transition and the LPB $E_X - E_{LPB_{k=0}} = 20meV$ confirms that the strong coupling is preserved over threshold. This feature agrees with the very small Bohr radius of the exciton in ZnO which lower the polariton-polariton and X-X Coulomb interaction in comparison with e.g. GaAs.

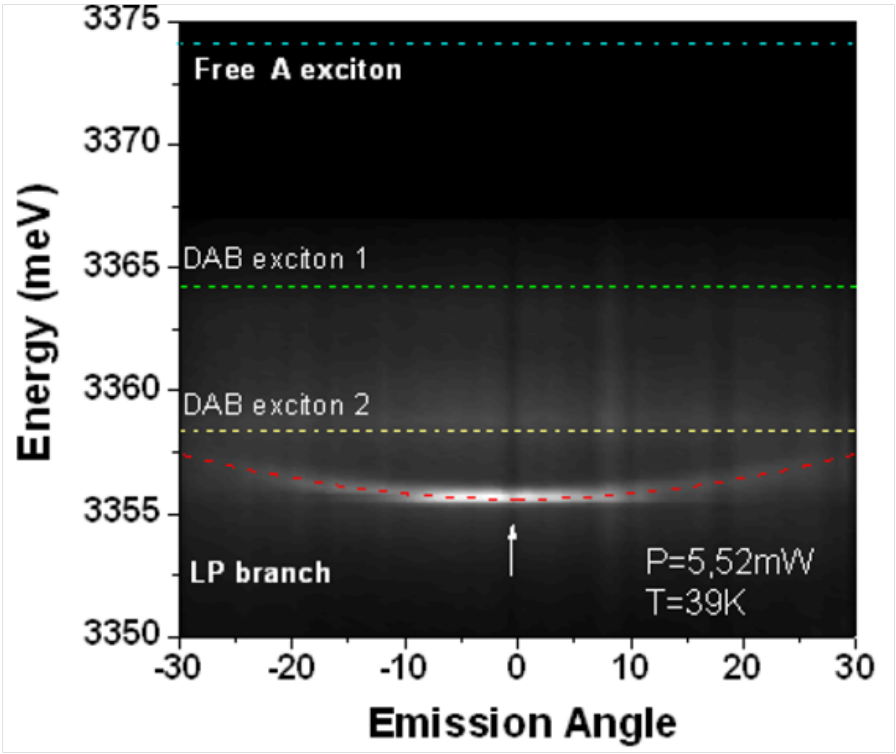

Figure 1.15: Angle resolved photoluminescence spectrum of the 97% excitonic lower polariton branch over threshold.

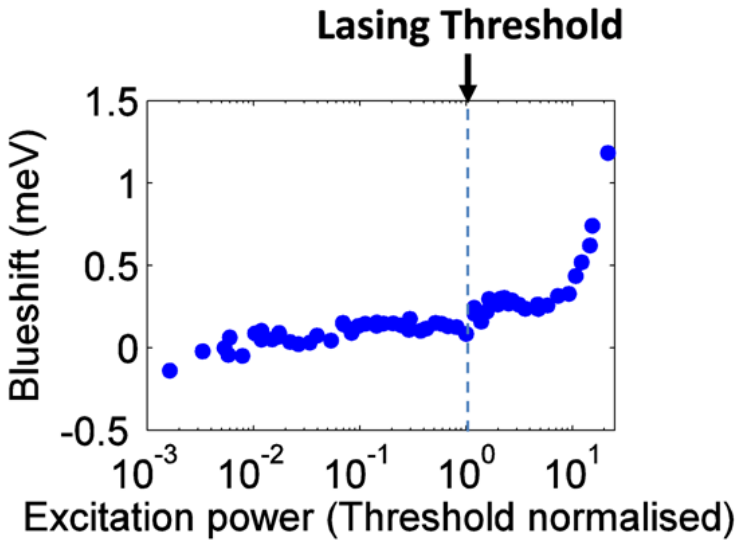

Figure 1.16: Evolution of the blueshift of the polariton state versus the pump power at 10K.

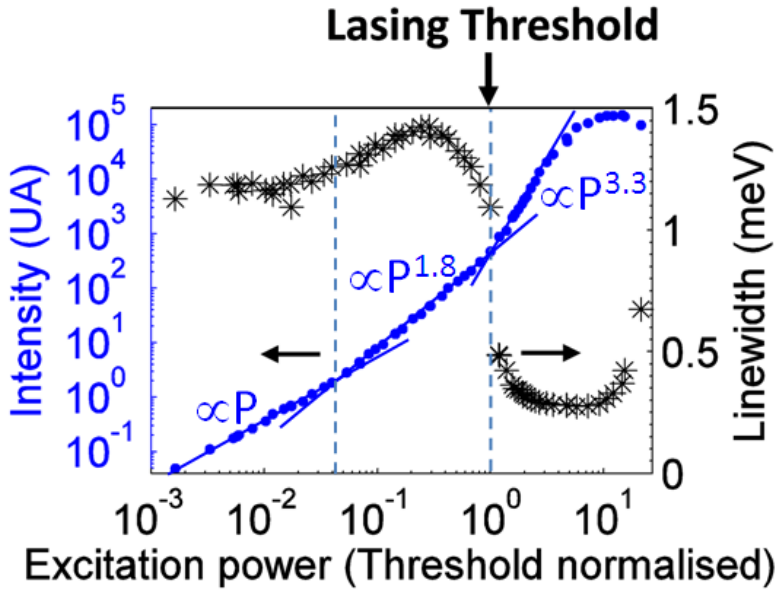

Figure 1.17: Evolution of the linewidth of the polariton mode versus the pump intensity at 10K.

As it is shown on Fig. 1.17 at low excitation power, the linewidth of the mode remains constant and the intensity increases linearly with the excitation power. This regime corresponds to a phonon assisted scattering of the reservoir excitons to the polariton mode. By increasing the pumping power, the system reaches an intermediate regime in which two body scattering in the excitonic reservoir begins to contribute to the dynamic. This leads to an increase of the linewidth coupled to a non linearity between pumping power P and intensity of the light emitted I going in $P^{1.8}$. By crossing the threshold, a much stronger nonlinearity $P^{3.3}$ shows up that we attribute to stimulated relaxation. At the same time, a dramatic narrowing of the linwidth appears as expected. At higher power (ten times the threshold power) where we did not checked that the strong coupling is preserved a qualitative increase of the correlations apppears coupled to a saturation of the emitted power.

Gain mechanism of the polariton laser As it was described in 1.3.4 , the microwires studied during that work are multimode photonic structures, and hence multimode polaritonic structures. This multimode nature is shown on the Fig. 1.12 and 1.13 . When increasing the pumping power further above threshold, the mode right below the first lasing one takes over and starts lasing as well followed by the one below and so on. The more striking peculiarity of the investigated polariton laser consist in the very high excitonic fraction of the lowest excitation power lasing mode which originates from

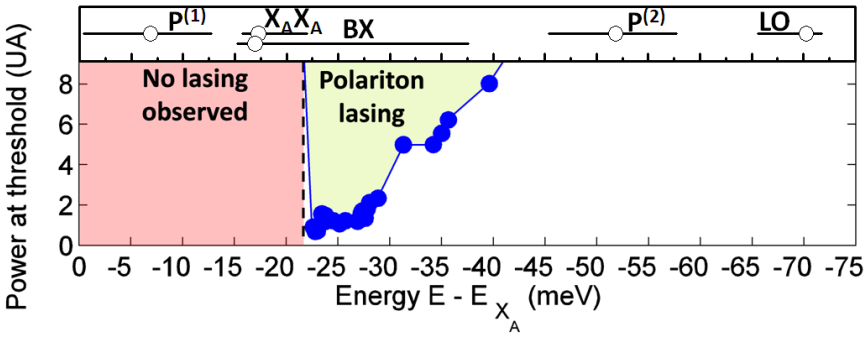

Figure 1.18: Gain mechanisms susceptible to be involved in the polariton condensate feeding (upper panel)Threshold power versus energy of the polariton laser (lower panel)

the microscopic feeding mechanism of the polariton laser. By considering the set of polariton mode displayed on the Fig. 1.12 and recording the threshold pumping power versus the energy of the lasing mode, one gets the results displayed on the lower panel of the Fig. 1.18. This threshold spectrum is quite peaked between -25 to -35 meV below the excitonic energy. By checking the conservation of energy and momentum in various scenarii, we can estimate the energy ranges of the scattering processes within the reservoir shown on the upper panel of the Fig. 1.18 The results of the above analysis coupled to the experimental data allow to conclude that biexcitons and or exciton-bound exciton scattering processes are involved in the mechanism feeding the polariton laser and rule out usually admitted feeding mechanism in ZnO such as exciton-exciton and exciton-LO phonon scattering.

1.4.5 Coherence properties of the one dimensional polariton laser

If the concept of thermal De Broglie wavelength is relevant in the case of a gas of cold atoms at equilibrium, it can't be defined in the case of polaritons because of the driven dissipative nature of those particles. Here is introduced the correlation length of the polariton which is the relevant physical length in the driven dissipative context. Then, we proceed with describing the coherence properties of the one dimensional condensate at cryogenic temperature. During that part the response function of the experimental apparatus will be determined, then the data below threshold will be discussed. In the end, the over threshold results will be presented and analyzed addressing the influences of pulsed excitation, interactions and disorder on the time integrated first order spatial correlation function.

Relevant parameters in the polariton case Polaritons are featuring a finite lifetime and are constituting a non equilibrated system in the driven dissipative regime. In their case, the thermal De Broglie wavelength is no more relevant. The relevant physical quantity is rather connected to the lifetime instead of to the temperature..

Here is given a simple way to define the lower bound of this correlation length of the polaritons. Let us consider the finite lifetime 97% excitonic polariton state, Γ_p its linewidth.

We can determine its extension in momentum Δk_{max} in the following way :

$$\frac{\hbar^2 k_+^2}{2m} = \frac{\hbar\Gamma}{2} \tag{1.28}$$

Thus:

$$\Delta k_{max} = k^+ - k^- = 2\sqrt{\frac{2\pi m\Gamma}{h}} \tag{1.29}$$

With the Heisenberg uncertainty principle, we can connect : $\Delta k_{max}(\Gamma)$ with the lower bound of the correlation length Δx as :

$$\Delta x \geq \frac{2\pi}{\Delta k_{max}(\Gamma)} \tag{1.30}$$

The investigated polariton state features a k_{max} value is of the order of $5\mu m^{-1}$.

In the end the lower bound of the correlation length is found to be of the order of $1\mu m$.

This has to be compared with the bare excitons mass is $1.77.10^{-31}kg$ in ZnO which gives a De Broglie thermal wavelength of $8.4.10^{-8}m$ at 4K.

The comparison of those values (lower bound of the correlation length of the 97% excitonic polaritons and De Broglie thermal wavelength for the excitons) allows to understand the strong influence of the 3% photonic dressing of the exciton provided by the strong coupling regime on its quantum degenerate regime.

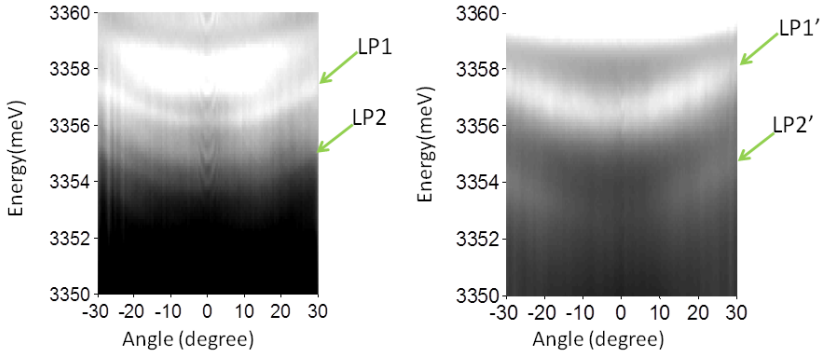

Figure 1.19: Angle resolved photoluminescence picture of the two regions where polariton lasing occurs and where the coherence properties have been probed.

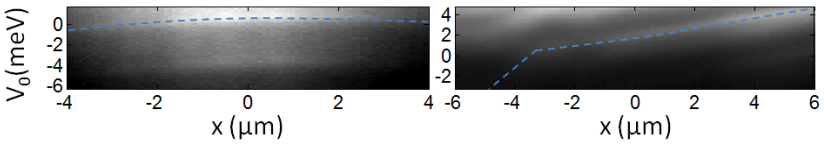

Figure 1.20: Space resolved photoluminescence picture of the two regions where polariton lasing occurs and where the coherence properties have been probed probed.

Description of the regions of interest The experiments have been performed on two different areas featuring a polariton mode entering the laser regime with a photonic fraction $|G|^2 = 2 \pm 1\%$, the dispersions of those two modes are presented on the Fig.1.19 On those dispersions one should note that the first mode to lase are the one respectively quoted LP2 and LP2', the higher energy ones (LP1 and LP1') are not lasing at 40K.

The Fig. 1.20 presents space resolved photoluminescence data of the two regions of interest which allows to properly determine the potential experienced by the polariton condensate. One should note that if the left panel potential is more or less flat, the right panel on feature a $dE/dx = 0.5meV\mu m^{-1}$ in both cases, the variation of the potential is attributed to a variation of the uncoupled HWGM mode energy along the wire axis.

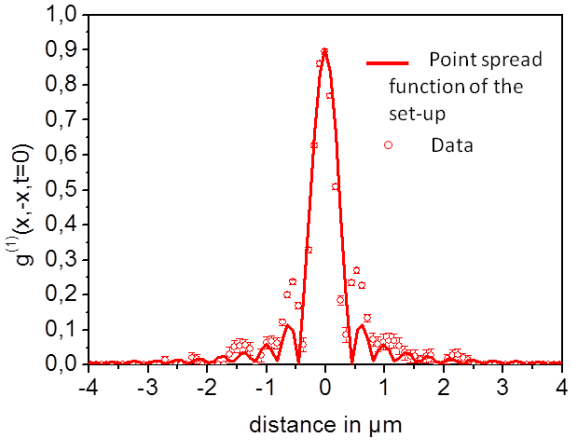

Figure 1.21: Modelisation of the response of the g1(x,-x,t=0)measurement setup probing a perfectly incoherent light source (solid line) and g1(x,-x,t=0) below threshold

Point spread function of the setup In order to accurately determine the spatial correlations of the polariton degenerate gas, a good knowledge of the response function of the experimental apparatus is needed. The solid line of the figure 1.21 presents the simulation of the point spread function of the setup probing a perfectly incoherent light source (i.e. delta correlated). In our case, we are using a $O = 0.5$ numerical aperture objective, the calculated response of the experimental apparatus reads as :

$$g^{(1)}(x,-x) = g_0^{(1)}(x,-x) = \frac{2J_1(2\pi xO/\lambda)}{2\pi xO/\lambda} \tag{1.31}$$

with J_1 the Bessel function of order one and λ the wavelength of the mode of interest.

$g^{(1)}$ below threshold Below threshold, the polariton gas behaves as a spatially extended incoherent light source. The multimode nature of the polariton gas (cf. Fig. 1.12) makes necessary to spectraly resolve the measurements , the analysis is performed for the mode of interest by only considering $g^{(1)}(x,-x,t=0)$ at the energy of this mode.

The figure 1.21 presents the experimental points (red squares) $g^{(1)}(x, -x, t = 0)$ obtained on LP2 below threshold superimposed with the theoretical setup point spread function .

The excellent agreement between the simulation and the experimental data proves that the spatial coherence is fixed by the point spread function of the setup mentioned before and that below threshold, the polariton gas correlation length is too short to be resolved.

Build up of long range spatial coherence

By increasing the pumping power, the modes of interest enters the quantum degeneracy regime. The Fig. 1.22 presents the interferograms $g^{(1)}(x, -x, t = 0, \omega)$ above threshold of the regions of the Fig. 1.20. The multimode nature of the polariton laser is clearly visible, the same energy selection as mentioned in 1.4.5 is performed. This spectral selection consisting in the selection of a narrow band in energy arround the horizontal red dashed lines of the Fig. 1.22.

The Fig.1.23 presents the experimental $g^{(1)}(x, -x, t = 0)$ of the two polariton lasers (red squares) superimposed with the below threshold $g^{(1)}(x, -x, t = 0)$ (blue squares).

A clear build up of long distance spatial coherence is visible in both cases, the range of this coherence exceeds $6\mu m$ in the case of the polariton laser of the flat potential (left panel) and $8\mu m$ in the case of the tilted potential. The difference between the two patterns is striking and will be addressed in the simulations.

1.4.6 Driven dissipatitive mean field model simulation

As mentioned in the introduction of the chapter this work has been realized in close collaboration with our colleagues of the Laboratoire de Physique et de Modélisation des Milieux Condensés who built a theoretical mean field model based on the Gross Pitaevskii equation for the condensate. This part briefly introduces the key points of this model and presents the results which coupled with the experimental ones allowed to the comprehension of the influence of the phase fluctuations, the disorder, and the interactions on the spatial correlation properties of the polariton condensates.

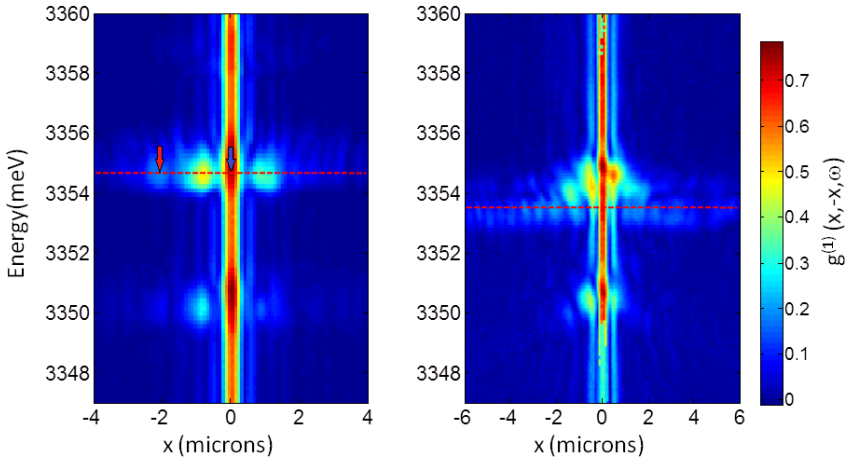

Figure 1.22: Interferograms $g^{(1)}(x, -x, \omega, t = 0)$ of the two regions of interest above threshold, the LP2 (left panel) and LP2' (right panel) polaritons are shown and the dashed lines are corresponding to the energy of the slices chosen to spectraly select the modes and extract the $g^{(1)}(x, -x, t = 0)$. The blue and red arrows are pointing on the pixels on which the contrast fitted on the Fig. 1.11.

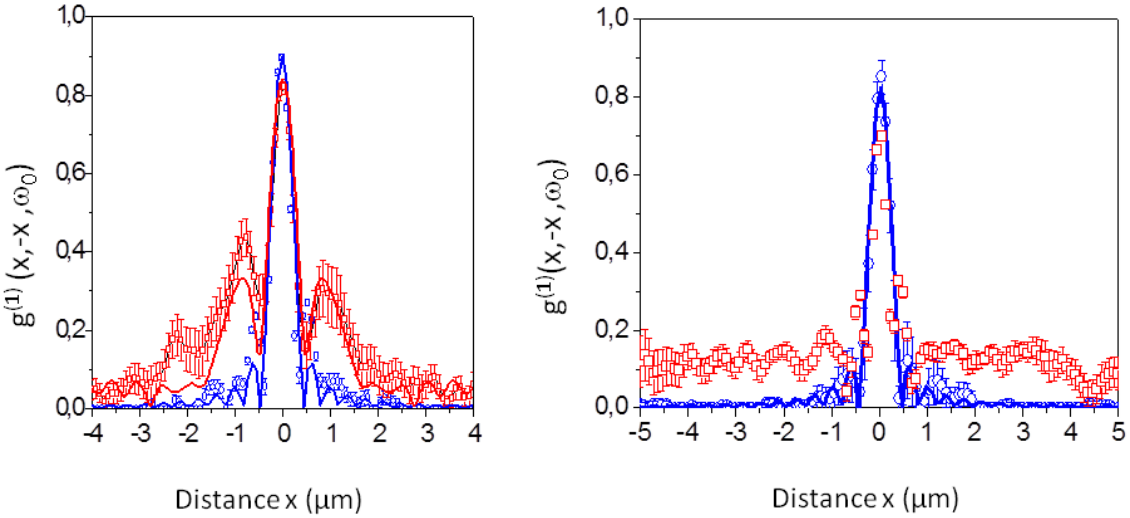

Figure 1.23: Experimental g1(x,-x,t=0) of the polariton gas (blue squares) below threshold and Driven dissipatitive mean field model simulation of the g1(x,-x,t=0) of the polariton gas (blue solid lines). and Experimental g1(x,-x,t=0) of the polariton condensate (red squares) over threshold and driven dissipatitive mean field model simulation of the g1(x,-x,t=0) of the polariton condensate (red solid lines). the left panel corresponding to LP2, the right one to LP2'.

description of the model The evolution of the polariton condensate wavefunction $\Psi(x,t)$ is described by the Gross-Pitaevskii equation with losses and gain:

$$i\hbar\partial_t\Psi(x,t) = -\frac{\hbar^2}{2m^*}\partial_x^2\Psi(x,t) + g|\,\Psi(x,t)|^2\Psi(x,t) + (V_r(x)+Ax)\Psi(x,t) + i(\lambda n_R^2(x,t)-\gamma_c)\Psi(x,t) \tag{1.32}$$

With respectively m^* the effective mass of the polaritons, g the interactions strength, γ_c being the condensate loss rate, $V(x)$ a random potential added to a tilted one Ax, mentioned in the previous part.

A reservoir $n_R(x,t)$ is feeding the condensate governed by the rate equation :

$$\partial_t n_R(x,t) = P(t) - \gamma_R n_R(x,t) - \lambda n_R^2(x,t)|\,\psi(x,t)|^2. \tag{1.33}$$

With λ the coupling with the condensate, $\gamma_R n_R$ the reservoir loss rate and $P(t)$ the pump rate.

In order to trigger the condensate dynamics, a low density seed is injected numerically in the wire such as:

$$\psi(x,t=0) = 5.10^3 cos(\pi x/L)exp(-(x-x_0)^2/l^2)exp(ik_0x) \tag{1.34}$$

L being the size of the system, x_0 the seed position, and k_0 the initial momentum.

The numerical resolution of the model assumes absorptive boundaries in space thus avoiding reflections of the condensate.

Theoretical results By only tuning L, x_0 and k_0 the model generates in both cases a spontaneously propagating condensate in agreement with the experimental data extracted from the Fig. 1.23, the parameter are respectively $L = 40$ µm and $l = -0.17L$ in both cases, $x_0 = -0.3L$, $k_0 = 89L^{-1}$ for the left panel of the Fig. 1.23, $x_0 = -0.4L$, $k_0 = 345L^{-1}$ for the right one.

The first result of this theoretical analysis confirm that thanks to the very small excitonic Bohr radius of ZnO exciton, the interaction strength is low enough to not play a role on the correlations. The Fig. 1.24 shows the influence of the interactions on

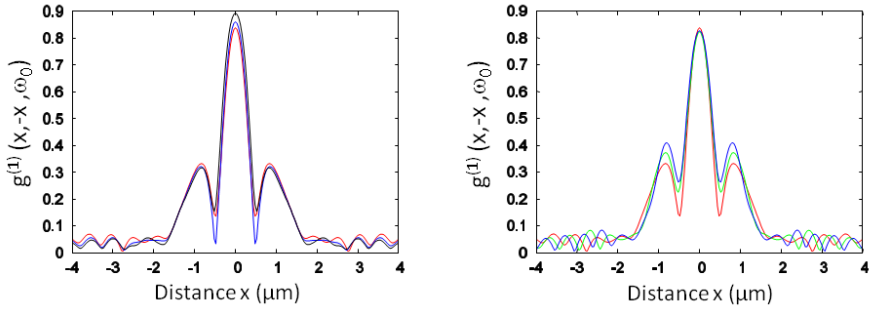

Figure 1.24: The left panel presents the simulated $g^{(1)(x,-x,t=0)}$ function with polariton-polariton interaction strength increasing and generating blueshifts going from $0\mu eV$(black line) to $25\mu eV$ (blue line) and to $50\mu eV$ (black line). On the right one, the parameters are the same as in the left one ( ) , but the reservoir-condensate interaction is added creating an additional blueshift [ ] going from $(0) + [0]\mu eV$ (blue line) to $(25) + [480]\mu eV$ (green line) to $(50) + [960]\mu eV$ (red line).

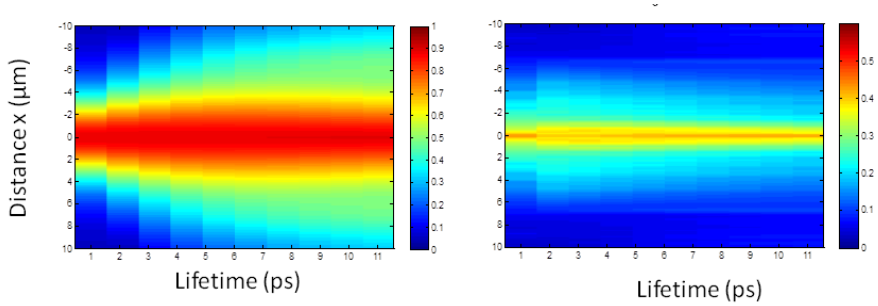

Figure 1.25: Driven dissipatitive mean field model results of the $g^{(1)}(x, -x, t = 0)$ of the polariton condensate versus polariton lifetime averaged over 15 disorder realizations and for a potential amplitude of variations $V_0 = 0.21mev$ a panel, and $V_0 = 2.28meV$ b panel .

the correlations of the system using parameters equals to the ones of Fig. 1.23. This influence of the interactions on the time integrated first order spatial correlation function of the condensate remains negligible since the blueshift remains below $50\mu eV$. The additional blueshift generated by the condensate-reservoir interaction is shown to not modify significantly the $g^{(1)}(x, -x, t = 0)$ function as well.

This demonstrates that the interactions are not modifying neither the shape, nor the range of the correlation function of the polariton condensate because they are dominated by the effect of the disorder.

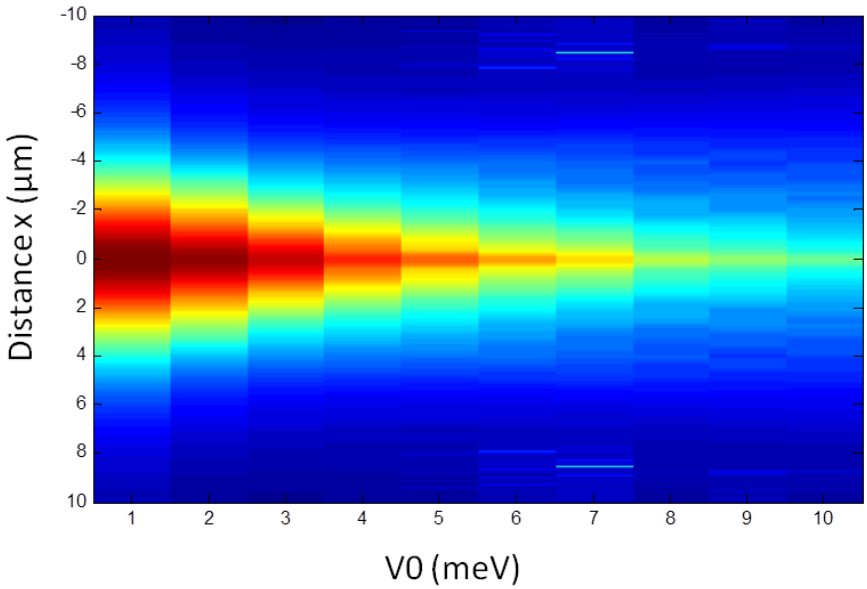

Figure 1.26: Driven dissipatitive mean field model results of the $g^{(1)}(x, -x, t = 0)$ averaged over 15 disorder realizations of the polariton condensate versus lifetime.

The Fig. 1.25 presents the calculated correlation functions versus lifetime averaged over 15 disorder realization for respectively $V_0 = 0.21meV$ and $V_0 = 2.28meV$ (resp. panel a and b).

If the polariton lifetime plays a key role in the case of a low disordered potential (i.e. disorder amplitude of the order of one tenth of the magnitude of the polariton linewidth) which correspond to the left panel of the Fig. 1.25, in the experimental frame, with a disorder amplitude of the order of magnitude of the polariton linewidth, the polariton lifetime does not influence the range of the spatial correlations.

The Fig. 1.26 presents the average over 15 disorder realizations of the calculated correlation functions for a given lifetime = 2ps versus disorder amplitude. The disorder amplitude has a strong influence on the range of the time integrated first order spatial correlation function.

1.4.7 Conclusion on the coherence properties of the measured one dimensional highly excitonic polariton condensate

The experimental results combined to the theoretical predictions allowed to understand that the decay of the correlations of the one dimensional polariton condensate investigated

during that work is due to propagation generated by the out-of-equilibrium nature of the condensate, under the combined effects of the random potential experienced by the condensate which breaks spatial inversion symmetry and the effect of the temporal average. The modulations are due to a shallow disorder of amplitude 2meV, i.e.comparable with the polariton linewidth.

In the investigated ZnO microwires the polariton lasing generates the formation of a one-dimensional weakly-interacting condensate of quasi-excitonic nature. Despite its very high excitonic fraction, the condensate features a coherence range comparable to the one obtained in 50% exciton-photon polariton condensates. This is allowed by the small excitonic Bohr radius in ZnO which decreases enough the polariton-polariton and polariton-exciton interactions combined with the large Rabi splitting.

1.5 Applications/ouverture : polariton application

An application of the ZnO polaritons studied in this work has been developed giving rise to a patent preparation. This application could not be presented in this manuscript for intellectual property reasons.

1.6 Conclusion

This chapter shown that despite the 97% excitonic fraction featured by the ZnO microwire one dimensional polariton laser, its spatial coherence range is of the order of magnitude of the ones commonly reported in planar microcavities with 50% excitonic fractions polaritons. The experimental results combined to the theoretical analysis allowed to understand that the shape and the decay of the $g^{(1)}(x, -x, t = 0)$function is determined by the effect of spatial phase fluctuations under the time average of the calculation of 1.25. Thanks to the very small ZnO excitonic Bohr radius, the interactions are not affecting significantly the condensate $g^{(1)}(x, -x, t = 0)$ correlation function. A potential application of the ZnO polaritons studied during that work is giving rise to a patent preparation.

Chapter 2

Using polariton as a coolant in 2D planar micro cavity

2.1 Introduction

This part describes the use of inelastic scattering of polaritons inside a 2D planar microcavity in the strong coupling regime that provides an all optical mean to lower the thermal vibrational energy of the solid state cavity, thus effectively cooling it down.

In this context, the mixed light-matter nature of the polaritons is an optimum situation : the polariton excitonic fraction is used to interact with the lattice vibrations, while the photonic one is used to lower the lifetime of the particles increasing by two order of magnitude the radiative rate in comparison with bare excitons and couples the polaritonic field inside the cavity to the photonic one outside. This provides a novel ultrafast cooling mechanism which is unique to polaritons.

This part describes the use of angle-resolved Anti-Stokes Raman spectroscopy to characterize how polaritons behave as a refrigerant gas for the phonon thermal bath. The strategy consists in the injection of polaritons in k=0, thanks to theirs excitonic component, a fraction of those polaritons absorbs a phonon before recombining. This process thus carry out of the microcavity the energy of the absorbed phonons.

After a description of the sample used to implement the ASF cooling strategy, the description of the experiments carried out will be given. The results and their analysis will be presented.

2.1.1 Generalities on Anti-Stokes Fluorescence cooling in solid state environment

Stokes and Anti-Stokes Raman processes correspond to inelastic scattering of light with phonons inside matter. From the thermal point of view, those two processes are leading to opposite effects. A Stokes process adds a phonon to the phonon bath and thus heats the solid up while an Anti Stokes one removes a phonon thus cooling down the solid:

- Stokes fluorescence consists in the emission of a phonon with an energy E_{phonon} by an excited state with an energy $E_{excited}$ before it recombines, the emitted photon energy is $E_{excited} - E_{phonon}$. It induces the addition of a phonon to the bath. This processes heats up the system.
- Anti Stokes fluorescence consists in the absorption of a phonon with an energy E_{phonon} by an excited state with an energy $E_{excited}$ before it recombines, the emitted photon energy is $E_{excited} + E_{phonon}$. It cools down the system by removing a phonon of the bath.

The Anti-Stokes Fluorescence (ASF) cooling exploited during that work uses this last characteristic of the light matter interaction to carry out phonons of a solid state system thus cooling it down.

In order to reach an efficient ASF cooling the material used must feature an electronic transition with a high radiative rate allowing a fast cooling dynamic, a high quantum efficiency (Since the Anti-Stokes fluorescence is competing with non radiative relaxation which heats up the system, the radiative channel rate must be much faster than the non radiative one) and a large coupling between the considered excitations and the phonons. Those conditions are hard to meet in real-life imperfect materials. The best results so far have been obtained in Ytterbium-doped crystals. Indeed, in spite of the long radiative lifetime and weak oscillator strength of the embedded Ytterbium atoms, their high quantum efficiency allowed cooling from room temperature down to $T = 110\text{K}$ [13].

In semiconductor materials, the excitonic transition has a much larger oscillator strength, a stronger coupling to phonons, and a shorter radiative rate. It was thus predicted that optical cooling in semiconductor should be much more efficient [76] [77]. However, despite encouraging results [78] [79] it is only recently that a room temperature ZnS nanoribbon has been cooled down to $T = 260K$ [14]. The difficulty lies in the fact that, owing to their extended nature, excitons are more prone to non-radiative relaxation

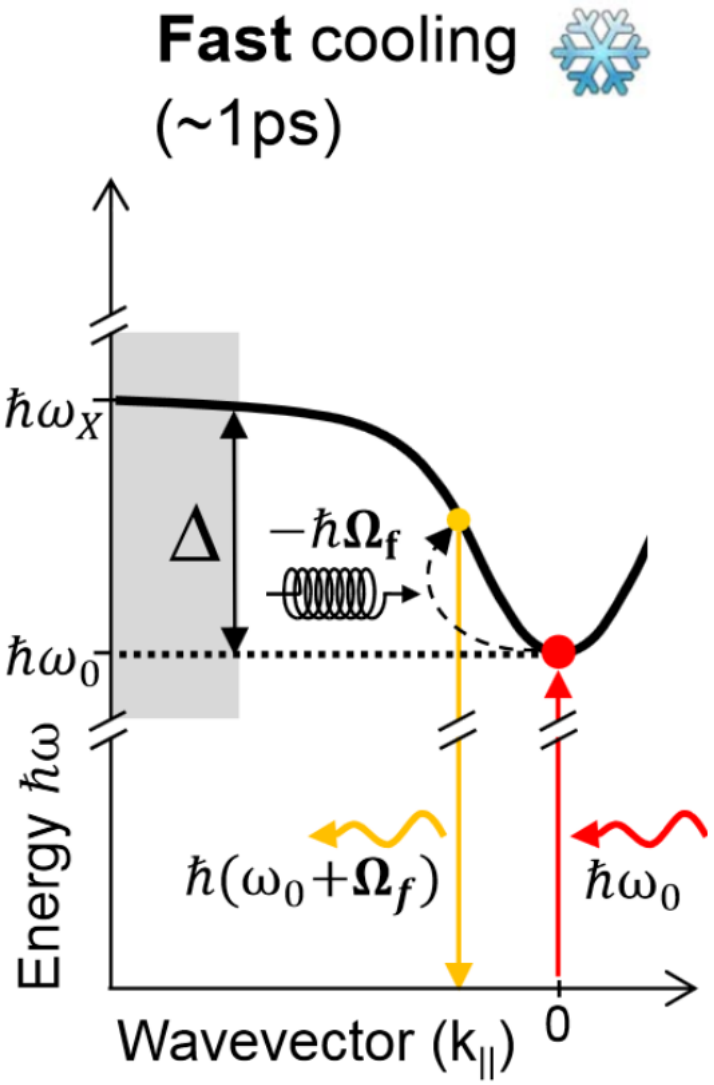

Figure 2.1: Schematic representation of the ASF polariton cooling.

via impurity or defect states, reinforced by the long-lived dark exciton states. Those relaxation channels involve phonon cascade emission [80] that competes with the phonon absorption achieved by ASF, making it hard to reach a positive net cooling power.

The short lifetime of polaritons coupled to their high quantum efficiency make them ideal particles to implement an ASF cooling strategy.

2.2 Polariton Anti Stokes Fluorescence cooling

The principle of polariton Anti Stokes Fluorescence (ASF) cooling is schematized on the Fig. 2.1, it relies on the injection of polaritons in the ground state (i.e. at $k_{\parallel} = 0$ and $E = \hbar\omega_0$) and on the fact that they are scattered at both higher energy and momentum by absorbing phonons, then they recombine emitting a photon which escapes the structure carrying out the thermal energy of the absorbed phonon and thus cooling the lattice down.

This section presents the generic properties of polariton ASF in the context of cooling. After the presentation of the advantages of the polaritons to implement this strategy, the different mechanisms involved in polariton ASF will be discussed.

2.2.1 Polariton advantages in the context of ASF cooling

First order Anti Stokes process : Thanks to the strong coupling regime, the direct Anti Stokes Fluorescence processes in which polaritons are involved (thereafter called polariton ASF) is a first order process : As shown on the Fig 2.1 the mechanism does not involve any virtual state and is described by the Fermi's golden rule applied at the first order.

Inhibition of Stokes fluorescence Thanks to the peculiar polariton dispersion, there are no available states below the LPB ground state. This fully inhibits the Stokes emission detrimental to cooling.

Continuum of energies reachable Thanks to the coupling between the bidimensional polaritons and 3D phonons, an energy continuum of final scattering states is available allowing to remove phonons of nearly arbitrary low energy of the bath : there is nearly no low temperature cutoff, the cooling properties of polariton ASF are maintained at low temperature.

Suppression of the scattering toward dark X states Owing to the large polariton-exciton splitting, scattering towards the dark exciton level is strongly suppressed as compared to a weak coupling situation.

Large ASF bandwidth Unlike excitons, thanks to the polaritons ultra-light effective mass, the maximum ASF bandwidth (i.e. the energy range where polaritons states are found within the light cone) is large and fixed by the Rabi splitting and the detuning(cf. Fig. 2.1)

Quenching of the interactions with point like defects Thanks to their very light mass (10^{-4} lighter than excitons) the polariton correlation length is at least two orders of magnitude larger than the excitonic Bohr radius cf. 1.4.5. Thus their spatial overlap with the point like defects of the lattice (like Schottky of Frenkel defects) is four to five orders of magnitude smaller than with excitons. This quenches the polariton interaction with point like defects of the lattice.

Cooling dynamics The cooling dynamics of the ASF process schematized on the Fig 2.1 is as fast as polariton lifetime which is of the order of 1ps in the studied microcavity, that value has to be compared with the $200ps$ lifetime of bare excitons in ZnSe [81].

2.3 Sample

As described in the previous part a large bandgap microcavity with a large Rabi splitting and that remains in the strong coupling regime over a large temperature range is needed to implement Polariton ASF cooling.

The sample grown for this experiment by our collaborators from Bremen university is a high quality Selenide-based microcavity similar to that used in ref. [82]. It displays a $\hbar\Omega_R = 29$meV Rabi splitting, and a perfectly stable strong coupling regime between $T = 5$K and $T = 150$K.

This section describes the peculiarities and the physical parameters of such a cavity.

2.3.1 cavities fabrication

With a binding energy of 40meV [82] when embedded in a quantum well, ZnSe excitons are able to remain stable up to room temperature. Moreover the large oscillator strength they feature allows a large coupling with light and makes this material particularly well suited for ASF cooling experiment.

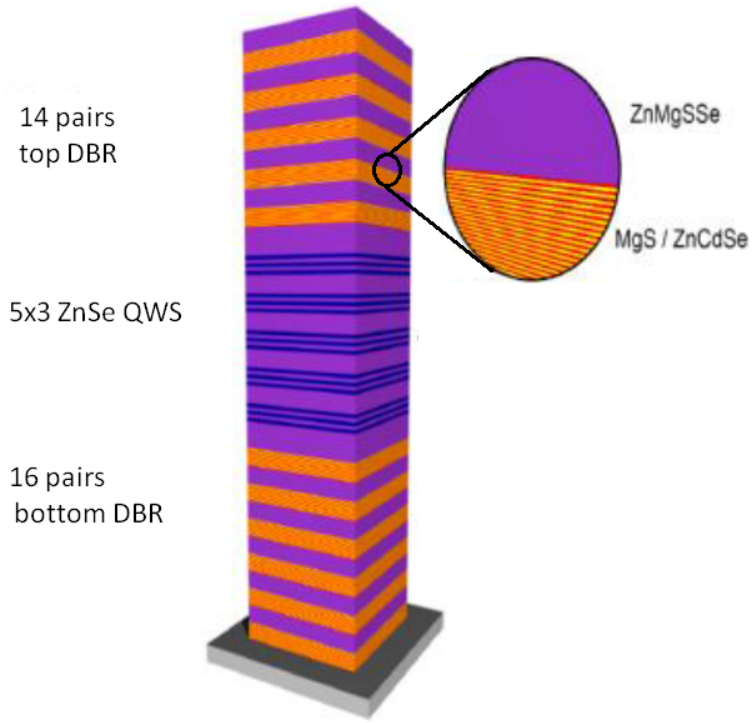

Figure 2.2: Schematic representation of the ZnSe cavities structure, adapted from [83]

The sample investigated during that work is a strong coupling regime microcavity that consists in a Fabry Perot resonator in which is embeded an excitonic medium (ZnSe quantum wells). The structure of such an optical microcavity is shown on the Fig 2.2. It shows the excitonic medium which is located at the position of the maxima of the intracavity field. This excitonic medium is embedded in a spacer material, this ensemble being located between two Distributed Bragg Reflectors.

The microcavity investigated during that work is fully monolithic and grown by molecular epitaxy.

The way the team of the university of Bremen uses to grow such a structure uses $ZnMgSSe$ quaternary material as a spacer as well as the barriers material, respectively $Zn_{0.72}Mg_{0.28}S_{0.29}Se_{0.71}$ as a high index material and a superlattice of $ZnCdSe/MgS$ as low index one.The excitonic medium is pure $ZnSe$.

All those materials are nearly perfectly latticematched with each other and feature a lattice parameter difference of only 0.37 % with the $GaAs$ substrate. The bandgap of the two high index and low index materials and the one of the spacer material must be higher than the one of the active medium in order to obtain the desired electronic confinement in the QWs. The selected materials are fullfilling this condition as shown on

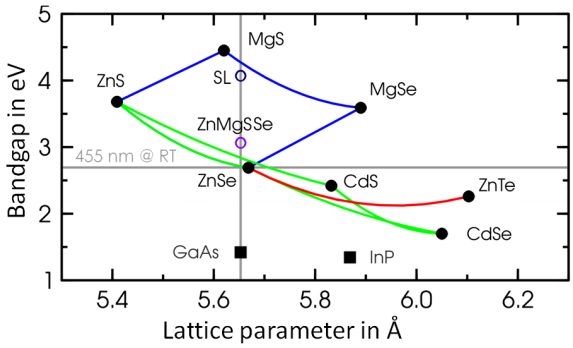

Figure 2.3: Bandgap versus lattice parameter of the materials used in the growth of the cavity SL stands for superlattice (adapted from [83]).

the Fig 2.3 which shows the dependency of the bandgap to the lattice parameter of the materials used in the growth of the cavity.

Transmission electron microscope and X ray diffraction studies performed on similar samples have shown that the crystalline quality of those sample is excellent and sets the state of the art for selenide heterostructures. [84] The Fig. 2.4 shows a Scanning Electron Microscope (SEM) picture of a structure similar to the one used in that work.

The MC studied during that work features five stucks of three ZnSe quantum wells embedded in the structure described previously cf. Fig. 2.2.

The light confinement of those structures is well known in the literature (see chapters 2 and 6 of [58]), the photonic confinement (in two dimensions in this case) induces a quantization of the perpendicular to the plane wavevector k_z which can be described as:

$$k_z = \frac{p\pi}{L_c} \tag{2.1}$$

with p the order of the Fabry Perot optical mode and L_c the effective optical thickness of the cavity.

$k_{\|}$, the component of the wavevector which is parallel to the plane is not quantized and we can describe the total wavevector as

$$\overrightarrow{k} = k_z\overrightarrow{u_z} + \overrightarrow{k_{\|}} \tag{2.2}$$

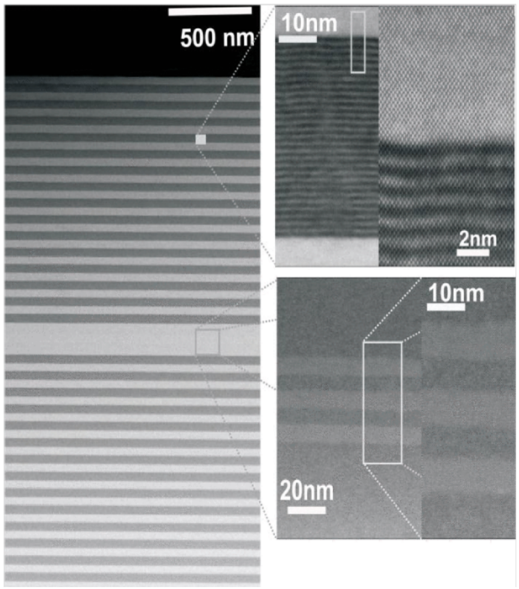

Figure 2.4: SEM pictures of the ZnSe structure : The left panel correspond to the full thickness of the microcavity, The upper right one is a zoom on the $Zn_xCd_{1-x}SeMgS$ superlattice, the lower right one shows the quantum wells adapted from [82].

Which defines the energy of the mode as a function of $k_{\parallel}$ such as:

$$E(k_{\parallel}) = E(k_{\parallel} = 0) + \frac{\hbar^2 k_{\parallel}^2}{2M^*} \tag{2.3}$$

With n_c the cavity refractive index.

One should note that this confinement gives a parabolic like relation of dispersion to the photonic mode around $k_{\parallel} = 0$ allowing to define an effective mass to the photon.

$$M^* = \frac{E_0 n^2}{c^2} \tag{2.4}$$

In these structures, the confined photon is in the strong coupling regime with the ZnSe quantum wells excitons. The eigenmodes are thus exciton-polariton .

The thus obtained planar microcavity features a quality factor of 5600 and thanks to the large oscillator strength and excitonic binding energy, it displays a 29 meV Rabi splitting and the strong exciton-photon coupling is preserved up to 150K.

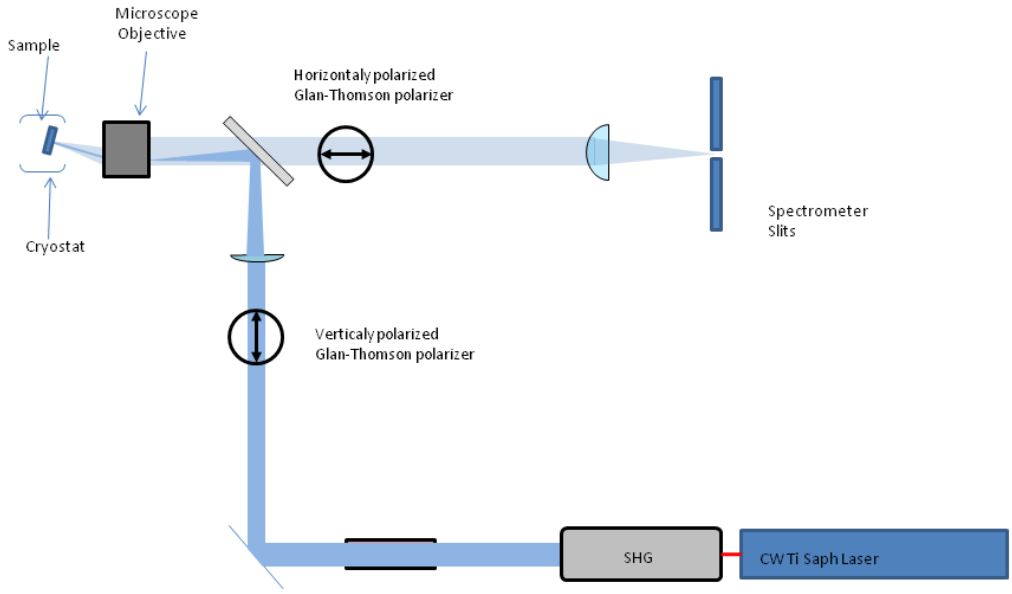

Figure 2.5: Overall scheme of the injection part of the setup : .

2.4 Experimental setup

This part describes the injection and detection stages of the experimental setup used during that work. It details the filtering scheme developed to be able to detect the polariton ASF signal. The overall scheme of the setup is given on fig. 2.5.

2.4.1 Injection

The sample is mounted with an upward angle of 13° with respect to the excitation/detection objective optical axis. In this way, spurious reflections of the laser on the objective entrance lens are suppressed upon exciting at $k_{\|} = 0$ (cf. Fig. 2.6).

The numerical aperture of the objective is 0.5, the relative tilt between the objective and the sample allows to detect ASF polaritons from $7° - 8°$ up to an angle of 43°. A CW laser beam is injected at a normal incidence angle on the microcavity by focusing it

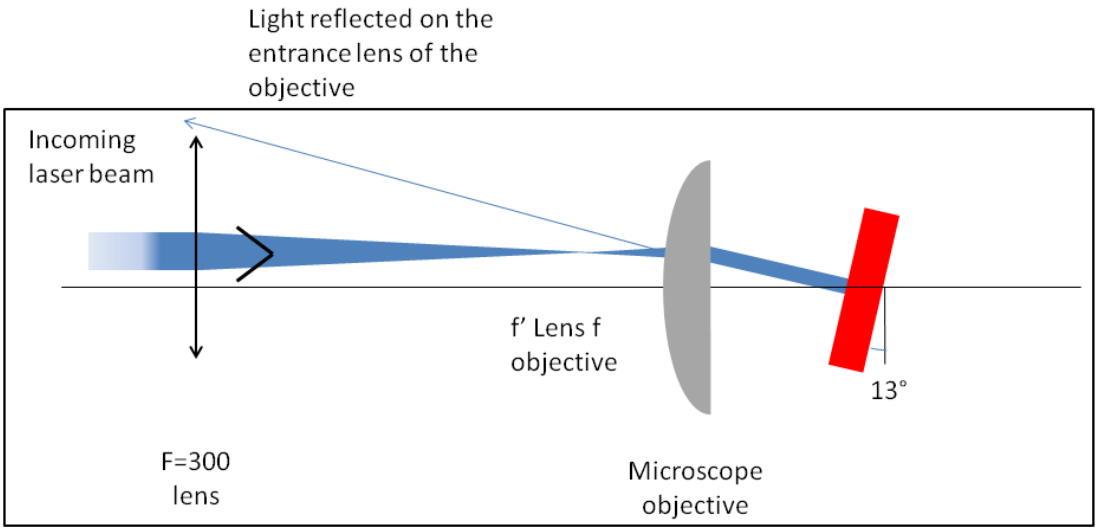

Figure 2.6: Scheme of the injection part of the setup : The laser beam is focalized in the focal plane of the microscope objective and slightly translated versus the optical axis of the objective, the output beam is almost colimated (the output beam divergence is 3°, and normal to the sample.

with a $f = 300$mm lens onto the input Fourier plane of the objective, so that a spatially Fourier transform excitation spot is achieved, with a diameter of 20μm on the surface of the sample with an angular spread of about 3°. The laser beam is tuned, angle-wise and in wavelength at resonance with the polariton ground state ($k_{\|} = 0, \omega_0$), at $\hbar\omega_0 = 2790$ meV. In this way, selective injection of polaritons in the ground state is achieved.

In the experiment deszcribed in this thesis, an energy difference $\Delta = \hbar(\omega_X - \omega_0) = 26meV$ between the polariton ground state ($k_{\|} = 0, \omega_0$) and the excitonic reservoir at T=5K is chosen. This $\Delta = 26$meV corresponds to an exciton/cavity detuning $\delta = (\omega_c - \omega_X)$ of $\hbar\delta = -17meV$ in order to minimize thermal excitations of excitons (inducing *slow* cooling mechanism) while conserving a significant excitonic fraction. This detuning opens up a large ASF bandwidth of 23meV, comparable with room temperature thermal energy (the Fig.2.7 schematizes those parameters).

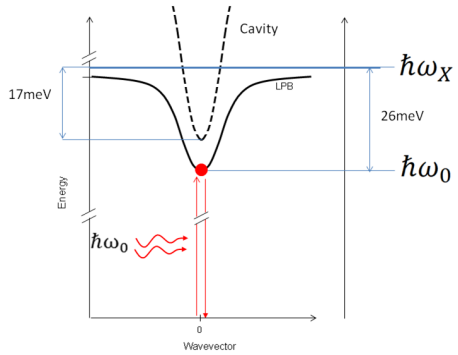

Figure 2.7: Scheme of the respective energies of the cavity, exciton and of the detuning exploited during the experiment.

2.4.2 Detection filtering

The excitation laser and the detection are cross-polarized by Glan-Thompson polarizers, thus achieving a rejection efficiency of 10^7. In this way, while the laser is fully suppressed with respect to the ASF intensity, a bright cross-polarized polariton emission still occurs from the ground state, likely due to a weak local spin-anisotropic disorder. This resonant photoluminescence is three orders of magnitude weaker than the incoming laser but still three to four orders of magnitude brighter than the ASF. To further reject this signal, two consecutive filtering steps are used : the Fourier plane is imaged on the slit of the monochromator, and a small region around $k_{\parallel} = 0$ is shifted away from the slit (cf. left panel of Fig. 2.8) The remaining spurious resonant signal is shifted away spectrally from the edge of the charged coupled device (CCD) sensitive area (cf. right panel of Fig. 2.8). Overall these filtering steps cuts emission angle from 0° to 8°, while we can measure ASF from 8° to 43°.

In order to further reject the excitation laser light, a fixed $k_x > 0$ is chosen and the resulting spectrum is also filtered from its lowest energy components. As a result, the ASF emission below $\theta_l = 8.4°$ ($k_{\parallel,l} = 2.1\mu\text{m}^{-1}$) is rejected (white stripe at the bottom of Fig. 2.9).

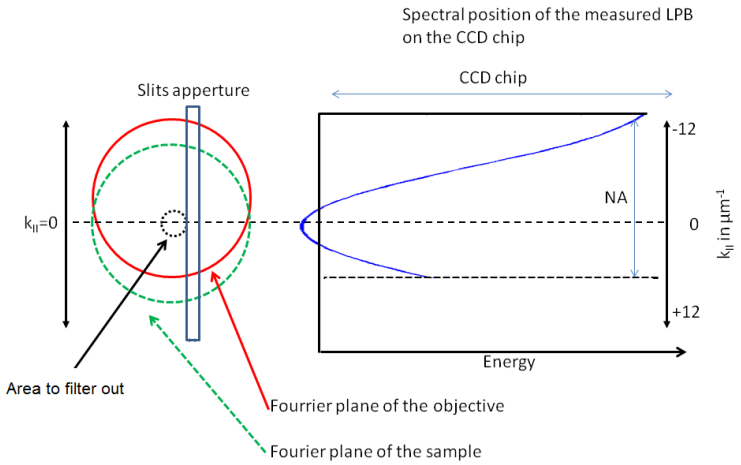

Figure 2.8: Scheme of the spatial(left panel) and spectral (right panel) filtering steps implemented in order to increase the signal to noise ratio

2.4.3 Detection probability

An absolute calibration of the setup detection probability is performed in the following way: a calibrated silicon photodetector is placed after the last beamsplitter, that provides a reading of the laser power P_1 at this point of the setup. The power actually entering the microcavity is $P_{\text{las}} = P_1 T_{\text{obj}} T_{\text{pol}}$, where $T_{\text{obj}} = 0.75$ is the objective transmission at $\hbar\omega_0$ and $T_{\text{pol}} \simeq 1 - R_{\text{pol}}$ is the measured microcavity transmission at resonance. Then the optical efficiency of the setup is calibrated using a reflection of the laser on the microcavity at a wavelength redshifted from the polariton resonance where it behaves as a $\sim 100\%$ mirror. Using again a calibrated photodetector allowed to determine that when a photon is emitted by the microcavity within the detected emission cone, it has a probability of 1.11% to be detected on the CCD. In other terms, at this wavelength, a conversion efficiency of 2.48×10^{10} counts/s on the CCD is found per μW of fluorescence.

2.5 Typical ASF spectrum and polariton ASF involved mechanisms

The Fig 2.9 shows a typical polariton ASF angle resolved spectrum (a detailed and commented description of this ASF signal will be provided thereafter). The ASF signal

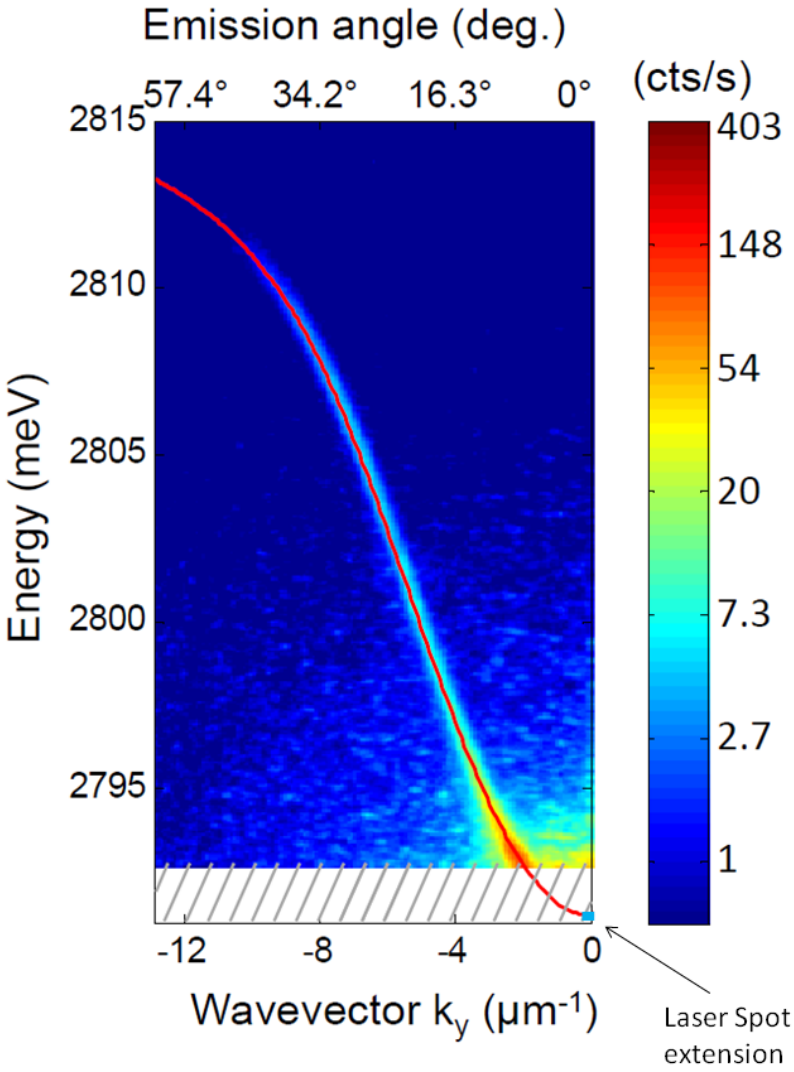

Figure 2.9: Typical angle resolved ASF spectrum at T=20K in logarithmic colorscale versus k_y and $\hbar\omega$ the red line is a fit of the polariton dispersion and the blue bar schematize the momentum width of the excitation laser. The hatched part at the bottom of the spectrum correspond to the filtered area.

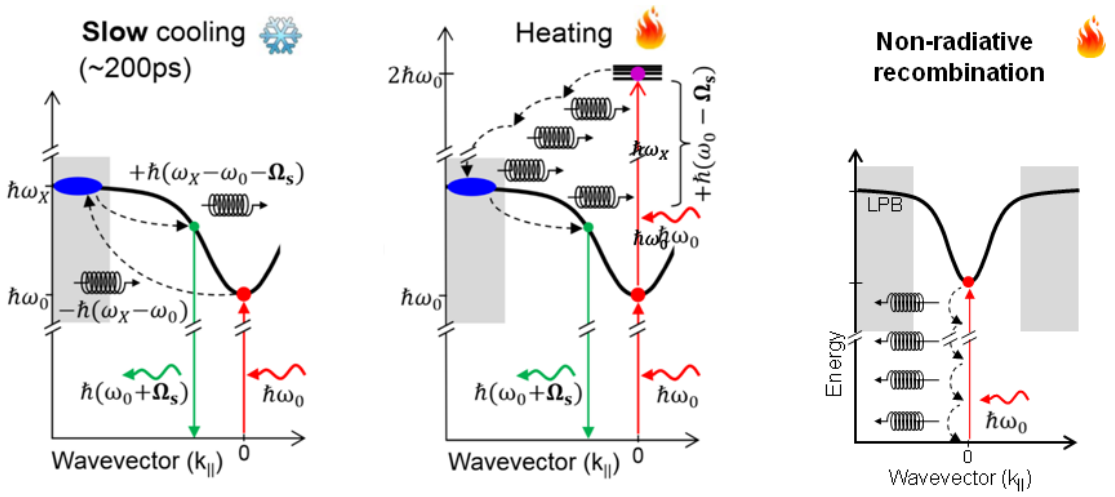

Figure 2.10: Schematization of the three ASF process : the left panel describes the slow process, the central one the heating by two photon absorption process and the right one the heating by non-radiative recombination of pumped polaritons of energy $\hbar\omega_0$. The intermediate states of the cascade are point-like defects in the crystalline structure. The multi-phonon cascade generates a total thermal energy of $\hbar\omega_0$ in the phonon bath

is clearly visible : the thermal phonons are scattering polaritons at both higher energy and momentum along the polariton branch. In the upcoming analysis, we found that this ASF signal actually has three distinct contributions. Two of them thereafter called *fast* and *slow* cooling process are cooling down the cavity, the third one is responsible for heating up the solid as it is adding phonons into the system and heats it up. This part describes those three processes and determines the average contribution of each of them to the thermal balance of ASF, in the end, non radiative recombination (NRR) is also considered, as another source of heat, and its effect on the total cooling power is estimated.

The fast process is that already described in the beginning of this chapter : it corresponds to the absorption of a low energy thermal phonon of energy $E_f = \hbar\Omega_f$ by a ground state ($k_\parallel = 0$) polariton of energy $E_{pol(k_\parallel=0)} = \hbar\omega_0$ which is scattered directly into an excited polariton of average energy $\hbar(\omega_0 + \Omega_f)$ within the light cone and recombines radiatively within a timescale of $1ps$. A schematic representation of this process is displayed on the Fig. 2.1 .

This process extract an average net thermal energy of $E_f = \hbar\Omega_f$ at each such event.

The Slow process uses the excitonic reservoir (outside the light cone) as an intermediate state : a ground state polariton absorbs a phonon of energy $E_f = \hbar(\omega_X - \omega_0)$ energetic enough to scatter it to the excitonic reservoir, where it stays for a "long" time ($\simeq 200ps$) it then relaxes back into the polariton state by emitting a phonon of energy $E_f = \hbar\omega_X - \omega_0 - \Omega_S$, relaxes into the light cone and then recombine emitting a photon. The net balance of this process is the removing of a phonon $E_{Slow} = \hbar\Omega_S$ The left panel of the Fig. 2.10 gives a schematic representation of the slow process.

In order to lower the participation of this slow dynamic process in the ASF cooling, one needs a large energy difference between the polariton ground state and the exciton thus decreasing the fraction of the phonon population able to scatter ground state polariton into the exciton levels. This separation is set by the detuning and the sample Rabi splitting which thus needs to be large.

Heating by two-photon absorption : There is a detrimental process to the cooling provided by ASF that has to be taken into account. Because of the non linear optical response of the excitonic medium, two photon absorption can takes place, that creates a hot electron-hole pair that relaxes to the excitonic reservoir by emitting a cascade of phonons, and then relax to the polariton branch by emitting a phonon. The central panel of the Fig. 2.10 schematize this heating process. One should note that this two photon absorption depends non linearly on the intra cavity field and scales like $1/\gamma^2$ (where γ is the linewidth of the uncoupled cavity mode) and could be decreased by lowering the quality factor of the cavity.

Non-Radiative Recombination is a process where an excitation (a pump polariton in our case) relaxes its total energy in the form of a cascade of phonons, involving localized defect states lying in the material bandgap (cf. right panel of Fig. 2.10). It is thus a source of heat. Owing to their largely dominant population, NRR of pump polaritons is the largest potential source of NRR in our microcavity. Since the NRR lifetime is around 6 orders of magnitude longer than the polariton lifetime in the MC the NRR rate measurement is quite challenging and its value has been estimated in the following way.

In order to estimate P_{NRR}, the contribution of pump polariton NRR to the heating power, the rough approximation that the polariton NRR rate γ_{nr} is that of exciton multiplied by the excitonic fraction X^2 is made.

Then, a simple rate equation model is used,

$$P_{\mathrm{NRR}} = P_{\mathrm{las}} X^2 \hbar\omega_0 \gamma_{\mathrm{nr}}/\gamma \tag{2.5}$$

With γ the polariton radiative rate.

To get an order of magnitude to compare with, the above estimation can be compared with the excitonic NRR rate $\gamma_{\mathrm{nr,X}}^{-1} = 350\mathrm{ns}$ found for ZnCdSe QWs excitons in ref. [85] which was measured at T=$50K$.

Several structural arguments are justifying a reduced NRR:

- Our microcavity is a fully epitaxial and the material of our QWs is binary ZnSe, so that the defect density within the QW is thus much lower than a for the $Zn_{0.50}Cd_{0.50}Se/Zn_{0.21}Cd_{0.19}Mg_{0.60}Se$, n-doped quantum wells ternary material employed in [85].
- The investigated QWs have a thickness of $d = 8\mathrm{nm}$ and are thus twice thicker than the ones of [85]. Since most defects leading to NRR are formed at the interface between the QW and the barrier, an approximately twice lower defect density is expected.
- TEM investigations of the MC have been carried out, including the QWs. The defect density which is found is indeed qualitatively very low and sets the state of the art for epitaxial II-VI materials [84].
- The electron donor responsible for the n-doping used in [85] provides non-negligible density of defect state, possibly contributing to NRR.

In our case, the excitations are polaritons instead of excitons, in the comparison above, it is assumed that the coupling between a polariton and a defect state is only reduced by a factor X^2 as compared to an exciton thanks to the half exciton-half photon nature of the polaritons. ,

However, considering the polariton mass typically four orders of magnitude lighter than the exciton one and by considering the result of 1.4.5, the polariton-point like defect spatial overlap is thus of the order of 10^{-3} times the one of excitons. According to the Fermi golden rule, its capture by a point-like defect of a size comparable with the lattice parameters must be reduced by the same order of magnitude.

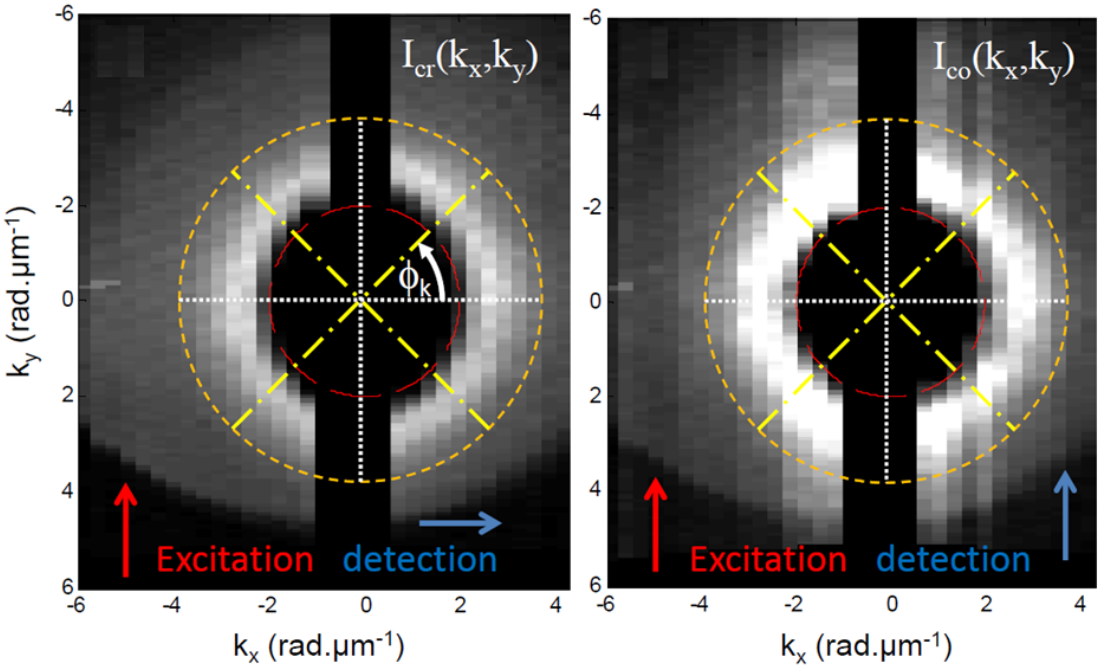

Figure 2.11: Spectrally-integrated cross-polarized $I_{cr}(k_x, k_y)$ (left panel) and co-polarized $I_{co}(k_x, k_y)$ (right panel)(ASF emission at $T = 50$K in $k_{\|}$-space. The hole in the middle (inside the red dashed line) is caused by the method for laser filtering. Inside the area encircled by the red and orange dashed line, *fast* ASF constitutes at least 50% of the counts.

Those arguments are confirming that the actual NRR lifetime $\gamma_{\mathrm{nr}}^{-1}$ in the investigated MC exceeds significantly 1500 ns.

2.5.1 Polarization properties of the polariton anti-Stokes fluorescence

In order to quantitatively access the thermal fluxes involved in the ASF cooling, the ASF polariton polarization properties must be understood : it has a major effect on the measurements since the detection part of the setup is cross polarized with the laser in order to reject the excitation laser. This part determines quantitatively its role in the ASF signal detection.

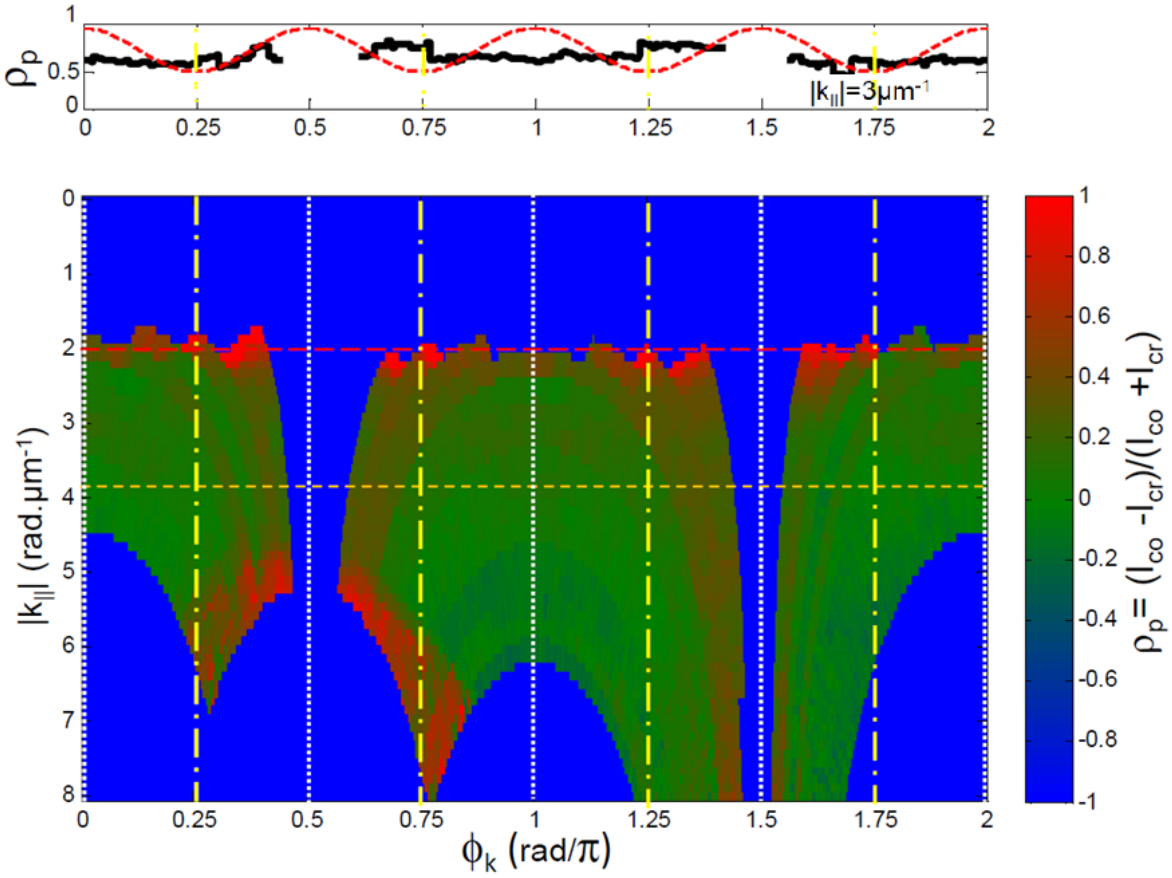

Figure 2.12: Upper panel : black solid line, measured degree of linear polarization $\rho_{\mathrm{P}}(\phi_k)$ for $k_{\|} = 3\mu\mathrm{m}^{-1}$. The red dashed line shows the theoretical linear polarization degree (assuming 50% of ASF) expected assuming only the effect of the TE/TM splitting on the anti-Stokes scattering. Lower panel : measured degree of linear polarization $\rho_{\mathrm{P}}(\phi_k, k_{\|})$. Green means depolarized. The solid blue area corresponds to points beyond the detection area. Its wavy irregular boundary is due to the sample tilt $\theta_t = 13°$ with respect to the objective optical axis. .

For the *slow* cooling mechanism and the two-photon absorption related fluorescence, a depolarized emission is expected since reservoir excitons and a fortiori hot free carriers undergo a fast spin scrambling. Therefore the cross-polarized detection scheme used during that work allows to measure one half of the counts of such origins.
In the *fast* cooling mechanism, a pump polariton is scattered into an excited polariton by absorption of a single thermal phonon. In principle, in this inelastic scattering process, polariton spin flip is strongly suppressed as compared to bare excitons. The reason is the following: acoustic phonons are lattice deformations that do not interact with the carriers spin. They do not interact either with the electron orbital momentum since the latter has a s-like symmetry. The hole orbital however, is p-like and lattice deformations can thus couple different hole orbital states with each other . As a result, an acoustic phonon can turn a $J_z = 1$ polariton into a $J = 2$ dark exciton, but it cannot directly turn into another $J_z = -1$ polariton of opposite spin. Since excitons with $J = 2$ have to be an intermediate state in the polariton spin flip, the latter is largely inhibited by the fact that the $J = 2$ exciton level lies energetically close to the exciton bright state, and hence due to the magnitude of the Rabi splitting, very far from the polariton ground state.

A vanishing *fast* ASF signal in a cross-polarized detection scheme is thus expected. However, on the contrary, we measure a signal which is strongly depolarized and isotropic : the latter contributes by more than 50% in the wavevector area comprised between the red and orange dashed lines ($1\mu m^{-1} < k_{\parallel} < 4\mu m^{-1}$) in Fig. 2.11 and 2.12. Two mechanisms are responsible for this depolarization and isotropic character :

- The first one relies on the significant TE/TM splitting exhibited by semiconductor MCs due to the dielectric nature of the layers [86]. The one of the investigated MC is quite large (measured to be : 2.67×10^{-14} meV.m^2, not shown) and has a strong effect on the polarization of anti-Stokes polaritons during their lifetime. This interaction is at the basis of effects such as the optical spin Hall effect [87, 88] , where a coherent polariton field pumped by a linearly polarized laser at $k_{\parallel} > 0$ is scattered by disorder. The TE/TM splitting causes a spin precession along the four diagonal directions with respect to the laser polarization $\phi_k = [\pi/4, 3\pi/4, 5\pi/4, 7\pi/4]$ (yellow dash-dotted lines in Fig. 2.11), while the laser polarization is conserved along the four directions $\phi_k = [0, \pi/2, \pi, 3\pi/2]$ (white dotted lines in Fig. 2.11). A resonant excitation experiment demonstrating that this precession occurs as expected in our MC has been carried out. In the exploited cross-polarized detection scheme, the four lobes where spin precession takes place are clearly visible along the four diagonal

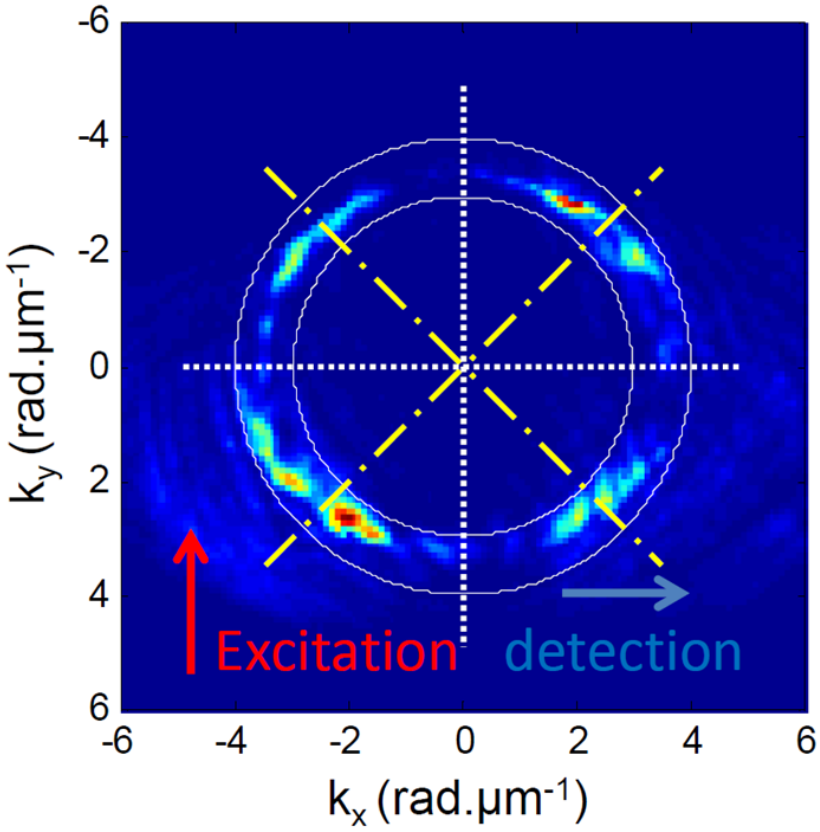

Figure 2.13: Cross-polarized resonant fluorescence intensity, for laser excitation at $k_{\parallel} = 3\mu\text{m}^{-1}$. The four lobes are clearly visible confirming the spin precession along the four diagonal directions. The corresponding integrated intensity $I_{\text{R}}(\phi_k)$ of the fluorescence inside the white lines bounded ring is plotted in the fig 2.14

directions (cf. Fig. 2.13), the integrated measured intensity $I_{\text{R}}(\phi_k)$ is shown on the Fig 2.14.

For anti-Stokes polariton, a very similar behavior is expected, except that since the laser coherence is lost in the scattering process, the spin precession is replaced by a depolarization along the diagonal directions. The linear polarization degree should thus look like the red dotted line in the upper panel of the Fig. 2.12 four lobes of depolarized light along the diagonal directions, and fours lobes of colinearly polarized light along the four other directions. However, the measured degree of polarization $\rho_p(\phi_k)$ is shown as a black solid line in the same plot: it is mostly flat, with no such lobes. This consideration allows to understand how depolarization occurs for half of the scattered polaritons but a second mechanism needs to be involved to explain the measured $\rho_p(\phi_k)$.

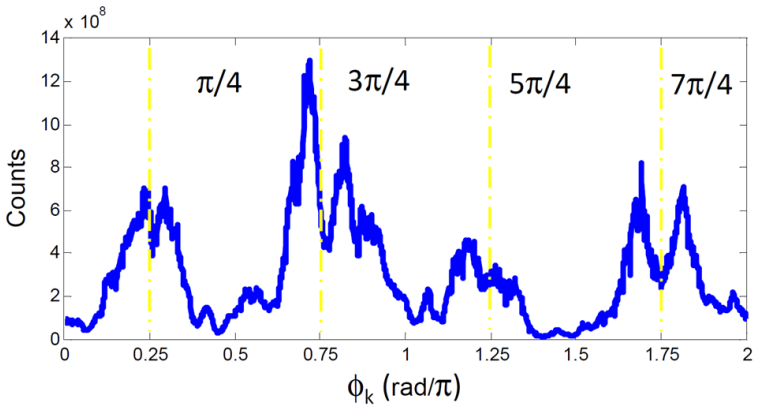

Figure 2.14: Integrated intensity $I_{\mathrm{R}}(\phi_k)$ of the fluorescence inside the white lines bounded ring of the Fig 2.13.

- The second is the consequence of the strong interaction that occurs between anti-Stokes polaritons and the the MC in-plane disorder. In this case, the depolarized polaritons gets scattered over every directions isotropically (Rayleigh scattering), while linearly polarized polaritons gets depolarized in the process, since this scattering mechanism is also affected by the TE/TM splitting. This additional step thus results in a fully depolarized *fast* polariton ASF.

This depolarization process of *fast* ASF is a useful advantage in the context of this work since, although the detection is performed cross-polarized with respect to the laser, only about one-half of the emitted photons are not detected for any of the cooling or heating mechanisms. Moreover, the isotropic character of the emission allows to extrapolate the total ASF from an incomplete measurement (a measurement along a single slice in momentum space, defined by the monochromator slit allows to reconstruct the full ASF emission).

2.6 Measurement of the thermal fluxes

The aim of the experiment is not to directly measure a temperature drop of the microcavity, which is dramatically prevented by the light-absorbing GaAs substrate on the sample backside, but instead to measure the detailed balance of the thermal fluxes generated

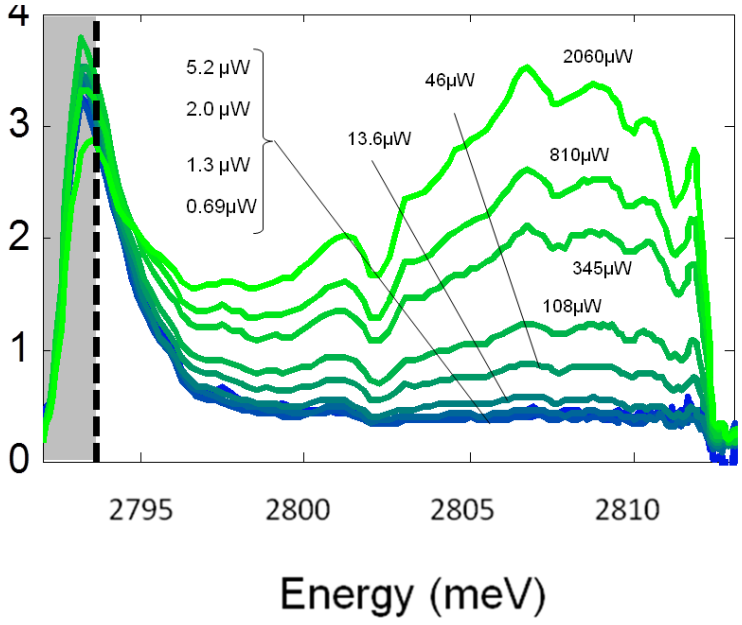

Figure 2.15: ASF spectral density divided by P_{las} in cts/s/meV/μW. Solid lines color evolves from blue to green for increasing leaser power P_{las}.

within the microcavity by the pumped polaritons. This part shows the results obtained using the angle-resolved anti-Stokes Raman spectroscopy setup described before on the ZnSe Microcavity introduced previously. The obtained results and their treatment is commented, the cooling efficiency of the polariton gas is then extracted.

2.6.1 Experimental method to count the extracted phonons

ASF polariton counting In order to get the polariton ASF count rate, I_{ASF}, the polariton dispersion of Fig. 2.9 is fitted, a mask is created that borders the raw dispersion (mask linewidth is set to 4 times the polariton linewidth) and rejects the surrounding noise. $i_{\text{ASF}}(\omega)$, the ASF count rate through the monochromator slit, is then obtained by summing up the counts along k_y. The total emission rate $I_{\text{ASF}}(\omega)$ is then extrapolated assuming an isotropic emission (cf. the part 2.5.1 of this chapter).

Finally, since we checked that ASF emission is isotropic, the total intensity of ASF $I_{\text{ASF}}(\omega)$ within a cone of $\theta = 43°$ radius is extrapolated. $I_{\text{ASF}}(\omega)$ normalized to the excitation power P_{las} is plotted in Fig. 2.15 for different P_{las}.

Determination of the linear and quadratic response of the ASF spectrum with respect to the laser power : The polariton ASF signal is the sum of two contributions respectively scaling like P_{las} and P_{las}^2. Here is detailed the way both of those contributions are quantitatively determined.

The fraction of the ASF spectrum that behaves linearly $A^{(1)}(\omega)$ and quadratically $A^{(2)}(\omega)$ with respect to P_{las} are obtained from the dataset $I_{\text{ASF}}(\omega, P_{\text{las}})$ shown on the Fig. 2.15 : for each energy pixel ω_n the data points $I_{\text{ASF}}(\omega_n, P_{\text{las}})$ are fitted with the function $A^{(1)}(\omega_n)P_{\text{las}} + A^{(2)}(\omega_n)P_{\text{las}}^2$.

The thus obtained $A^{(1)}(\omega)$ and $A^{(2)}(\omega)$ characterizes the ASF response to the optical excitation in counts/s/μW and counts/s/μW^2 respectively (cf. Fig 2.16). The error bars are obtained from the 95% confidence bound of this fitting procedure. This method allows an accurate separation of the two-photon absorption related source of heat, from the source of cooling, namely the *fast* and *slow* cooling mechanisms shown in Fig. 2.1 and Fig. 2.10.

In order to confirm the origin of $A^{(2)}(\omega)$ luminescence, a non-resonant CW experiment with an excitation laser tuned to $\lambda = 415$nm is performed, it allows to obtain the photoluminescence spectrum $I_{\text{PL}}(\omega)$ (solid red line in Fig. 2.16). $A^{(2)}(\omega)$ is found to have the same shape than $I_{\text{PL}}(\omega)$.

This leads to conclude that $A^{(2)}(\omega)$ results from two-photon absorption of the pump laser which generates high energy free carriers, that relax into the polariton states emitting a phonon cascade. This corresponds to the heating mechanism detailed on the right panel of Fig. 2.10).

From the thermal balance point of view, this mechanism is a source of pure heat since each absorption event adds a cascade of phonons of total average energy $\hbar(\omega_0 - \Omega_s)$ into the bath, where $\hbar(\omega_0 + \Omega_s)$ is the average energy of the non-resonant photoluminescence. Fortunately its quadratic behavior with P_{las} makes it vanish at excitation power low enough as we will see further.

Determination of the participation of fast and slow mechanisms to the ASF signal $A^{(1)}(\omega)$, the part of the spectrum which is linear with P_{las}, results from the absorption of thermal phonons by ground state polaritons of energy $\hbar\omega_0$ followed by fluorescence at higher energy than $\hbar\omega_0$. It thus provides the wanted cooling power, via the fast and slow mechanisms.

The respective contributions of fast and slow cooling mechanisms in the linear part of the ASF spectrum $A^{(1)}(\omega)$, could be separated using the fact that both mechanisms leads to very different spectra, in particular at the detuning choosen for the experiment where the non resonant polariton emission (as expected for the *slow* cooling fraction of the ASF) presents a strong bottleneck, i.e. an intensity maximum high above the ground state ($> 15meV$ in our case). The *fast* cooling fraction of the ASF is on the contrary peaked very close to the ground state and then decays quasi-exponentially with energy.

This separation is obtained from $A^{(1)}(\omega)$ by performing a spectral analysis : the *fast* ASF is a mechanism that involves a single scattering event between two polaritons state. Since the this scattering rate (polariton-phonon) is much smaller that the radiative lifetime [89], the corresponding ASF spectrum $I_{\text{th}}(\omega)$ can be accurately simulated within a Fermi-Golden rule approach. Our colleagues of the Laboratoire de Physique et de Modélisation des Milieux Condensés built a model simulating this response. The result, $I_{\text{th}}(\omega)$, is shown as the dash-dotted line in Fig. 2.16. It is peaked very close to the ground state (the maximum is not reachable experimentally because of the employed filtering setup) and vanishes quasi-exponentially for increasing energy.

Because it consists in an excitation of the exciton reservoir, the *slow* ASF spectrum is identical to that obtained under non-resonant excitations $I_{\text{PL}}(\omega)$: it exhibits a pronounced bottleneck $\sim$15 meV above the ground state.

$A^{(1)}(\omega)$ clearly features these two contributions: the upper flank of a high peak at the lowest energy (*fast* ASF) and a shoulder at higher energy (*slow* ASF). Using both $I_{\text{th}}(\omega)$ and $I_{\text{PL}}(\omega)$ to fit $A^{(1)}(\omega)$ (cf. blue solid line in Fig. 2.16), the fraction of *fast* cooling ρ contributing to the overall cooling power is evaluated. The accuracy of this procedure is guaranteed by the fact that $I_{\text{th}}(\omega)$ and $I_{\text{PL}}(\omega)$ have a poor spectral overlap.

In order to extract the fraction ρ of fast cooling in $A^{(1)}(\omega)$, the latter is fitted with the weighted sum of the non-resonant photoluminescence spectrum $I_{\text{PL}}(\omega)$ obtained by exciting the microcavity with a CW non-resonant laser at $2950meV$, and the ASF theoretical spectrum due to the fast cooling mechanism $I_{\text{th}}(\omega)$.

In the end, $A^{(1)}(\omega)$ reads :

$$A^{(1)}(\omega) = C\rho I_{\text{th}}(\omega) + C(1-\rho)I_{\text{PL}}(\omega) \tag{2.6}$$

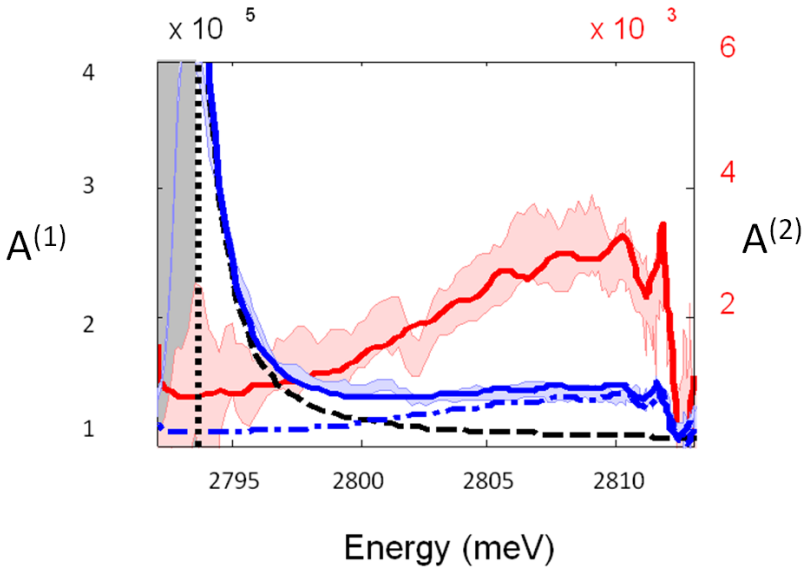

Figure 2.16: Measured (blue stripe) and fitted (solid blue line) linear component $A^{(1)}(\omega)$ of the spectrum in cts/s/meV/μW. Red: measured (red stripe) and fitted (solid red line) quadratic component of the spectrum in cts/s/meV/μW^2. The solid red line is proportional to $I_{\mathrm{PL}}(\omega)$. The dashed black line is the *fast* cooling component in $A^{(1)}(\omega)$, while the dash dotted blue line is the *slow* one. The data at energies below the black dashed line are modified by the filtering system used and are not related to the physics of the system.

with C a constant.

2.6.2 Determination of the thermal balance :

After having determined the relative weight of each of the process involved in the ASF signal, here is determined the net thermal balance of the polariton ASF cooling.

The average phonon energy absorbed by the fast cooling process goes like :

$$\hbar\Omega_f = \frac{\sum_n \hbar(\omega_n - \omega_0) I_{\mathrm{th}}(\omega_n)}{\sum_n I_{\mathrm{th}}(\omega_n)} \tag{2.7}$$

The average phonon energy absorbed by the slow cooling process goes like :

$$\hbar\Omega_s = \frac{\sum_n \hbar(\omega_n - \omega_0) I_{\mathrm{PL}}(\omega_n)}{\sum_n I_{\mathrm{PL}}(\omega_n)} \tag{2.8}$$

The average phonon energy absorbed by both cooling processes goes like :

$$\hbar\Omega_c = \frac{\sum_n \hbar(\omega_n - \omega_0)A^{(1)}(\omega_n)}{\sum_n A^{(1)}(\omega_n)} \tag{2.9}$$

The average phonon cascade energy emitted after a two-photon absorption process goes like :

$$\hbar\Omega_2 = \frac{\sum_n \hbar(2\omega_0 - \omega_n)A^{(2)}(\omega_n)}{\sum_n A^{(2)}(\omega_n)} \tag{2.10}$$

and since $A^{(2)}(\omega)$ has the same shape as $I_{\mathrm{PL}}(\omega)$, $\hbar\Omega_2 = \hbar(\omega_0 - \Omega_s)$.

The two photon absorption involved in this process involves a quadratic dependency to the excitation laser intensity and makes it negligible at low enough excitation laser power.

Since we have identified the three main mechanisms involved in the heat exchange between polariton and phonons, we can derive the total thermal energy removed from the microcavity (i.e. the fridge power) as

$$P_{\mathrm{fr}} = \int \mathrm{d}\omega \left\{ P_{\mathrm{las}}\hbar(\omega - \omega_0)A^{(1)}(\omega) - P_{\mathrm{las}}^2\hbar(2\omega_0 - \omega)A^{(2)}(\omega) \right\}, \tag{2.11}$$

With $\hbar(\omega - \omega_0)$ the energy of a phonon which has been removed when a photon is detected at the energy $\hbar\omega$. Positive P_{fr} means cooling while negative means heating. The cooling power P_{fr} has been extracted for temperatures ranging from $T = 4.2\mathrm{K}$ to $T = 150\mathrm{K}$. The result is displayed on the left panel of Fig. 2.17 versus temperature and laser power. Unlike other optical cooling methods, the maximum cooling power is found to be achieved deep in the cryogenic temperatures, at $T = 50\mathrm{K}$. This is possible because the ASF does not involve a discontinuous electronic density of state like in doped crystals but rather a bidimensional continuous one (polariton's) with no gap (unlike exciton-enhanced optical pumping) between the pumped and excited states. Therefore, phonons of arbitrarily low energy can in principle be pumped out from the thermal bath by this method.

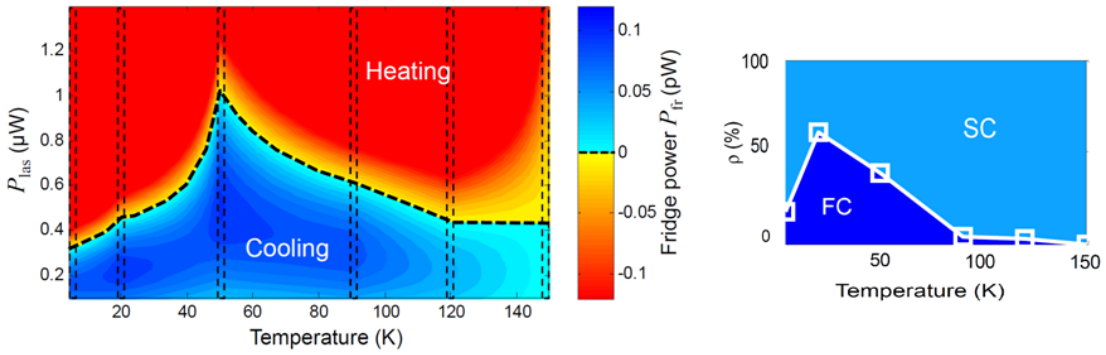

Figure 2.17: Left panel : Total fridge power versus cryostat temperature (T) and laser power P_{las}. The dashed line separate the cooling region from the heating one. The vertical dashed lines are showing the measurement temperatures. Right panel : Participation ρ of *fast* cooling (FC) (SC stands for *slow* cooling) involved in the overall cooling process.

2.6.3 Quantitative analysis of the thermal fluxes versus temperature.

Performing the above analysis at different cryostat temperatures between $T = 4.2K$ and $T = 150K$ allowed to determine the temperature dependency of *fast* and *slow* cooling mechanisms. The *fast* one has a peak contribution of $\rho = 61\%$ at $T = 20$K, and remains significant up to $T \simeq 100$ K (cf. Fig. 2.17, right panel). This *fast* cooling mechanism is unique to polaritons: its timescale is fixed by the polariton lifetime which is two orders of magnitude shorter than the *slow* cooling one. This dynamics is even faster than the phonons typical thermalization time [90].

The *slow* cooling mechanism is reminiscent from that involved in exciton-enhanced optical cooling [76]. At such low temperatures, its contribution can seem surprising as it involves thermal phonons of energy comparable with $\Delta \gg k_b T$. However, the weak phonon population at this energy is compensated by two aspects:

- (i) as stated by the Fermi golden rule, the polariton-phonon scattering rate scales like the final density of states (reservoir exciton's), which is four orders of magnitude larger than the one of polaritons.
- (ii) For such large Δ's the phonons involved are of the optical type, with a coupling matrix element with polaritons typically a hundred times larger than for acoustic.

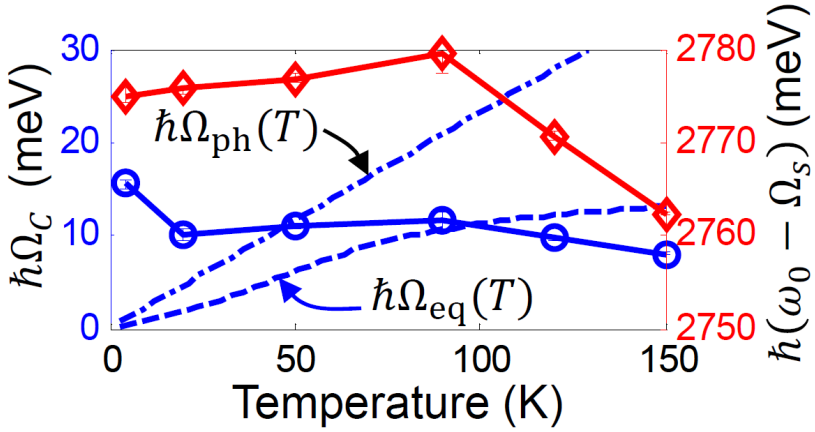

Figure 2.18: Red crosses: average energy $\hbar\omega_0 - \hbar\Omega_s$ of the phonon cascade involved in the two-photon absorption heating. Blue hollow circles: average phonon energy $\hbar\Omega_c$ removed by the overall cooling process. The dashed line shows the theoretical average energy of polaritons $\hbar\Omega_{\rm eq}(T)$ assuming thermal equilibrium with the phonon bath (same temperature T). $\hbar\Omega_{\rm ph}(T)$ is the average energy of thermal phonons.

The maximum cooling power is fount to be : $P_{fr}^{max} = (0.10 \pm 0.02)pW$ with $\rho = 40\%$ at T=50K

The average energy $\hbar\omega_0 - \hbar\Omega_s$ of the phonon cascade involved in the two-photon absorption heating and the average phonon energy $\hbar\Omega_c$ removed by the overall cooling process have been plotted versus temperature on the Fig. 2.18. The maximum achievable cooling power $P_{\rm fr}^{\rm max}$ is determined by the efficiency of two-photon absorption which releases an amount of heat as large as 2780meV per event. which sets the boundary (dashed line in the left panel of the Fig. 2.17) between the cooling and the heating region.

Discussion on the out of equilibrium nature of the polariton gas on the cryogenic properties. This work highlight an important aspect of the thermal properties of an out-of-equilibrium cryogenic fluid (polaritons) interacting with the phononic and excitonic bath over a timescale too short for polaritons to thermalize: they are injected in the microcavity at an effective temperature $T_{\rm eff} \simeq 0$K for the polaritonic sub-system. The outgoing polariton fluid (re-emitted by the microcavity) consists in two components: a fluid which is still at $T_{\rm eff} = 0$K, corresponding to polaritons that did not interact with phonons during their lifetime, and a second one, "heated up" by the interaction with phonons that produces the $A^{(1)}(\omega)$ fraction of the ASF. This "hot" component is completely out-of-equilibrium, with no definable temperature. In Fig. 2.18 the average

energy $\hbar\Omega_c$ of $A^{(1)}(\omega)$ versus temperature is plotted together with the theoretical one Ω_{eq} obtained assuming full thermal equilibrium of polaritons with the phonon bath (i.e. $\gamma = 0$ and Maxwell-Boltzmann distribution). Between $T = 0$K and $T = 100$K we find that $\Omega_c \gg \Omega_{\text{eq}}$, i.e. the energy removed per polaritons interacting with the phonon bath strongly exceeds that achieved with an hypothetical refrigerant at thermal equilibrium. In other words, the "hot" component is much hotter than the phonon bath. By giving polaritons more time to thermalize phonons, this "hot" fraction of the fluid would increase (thus increasing the overall cooling power) with respect to the non-interacting one, while Ω_c would decrease. This competition suggests that shifting a refrigerant fluid away from thermal equilibrium could enhance its cooling performance.

2.7 conclusion

This chapter shown an experimental proof of principle, that using Polariton Antistokes Fluorescence the cooling of a semiconductor microcavity can be achieved. The polariton specificities are allowing an efficiency of the dynamic of the cooling which is faster than the state of the art conventional ASF cooling realization : the very short lifetime of those particles being at the origin of the out of equilibrium nature of the polariton coolant. Thanks to the large Rabi splitting exhibited by our high quality sample, the energy difference between the polariton ground state and the excitonic energy limits dramatically the scattering toward the long lived excitonic states reinforcing the total net cooling power. The issue of the two photon absorption which is the limiting factor of the ASF cooling power could be solved by decreasing the quality factor of the cavity. On the same aspect, the *slow* process which slows down the overall dynamic of the ASF cooling could be completely inhibited by increasing the cavity Rabi splitting of a factor two. The obtained performances of this all optical way to cool down a solid state environment are very different from state-of-the-art demonstrations and might still be largely increased, opening the way to an experimental measure of the temperature drop under polariton ASF cooling.

2.8 perspectives

To summarize the measured characteristics of polariton cooling in this experiment, it has been found an optimum working point at ($T = 50K, P_{\text{las}} = 0.5\mu$W) including a

fast cooling participation of $\rho = 40\%$, that produces a rather modest cooling power $P_{\mathrm{fr}}^{\max} = 0.10 \pm 0.02 pW$. Both ρ and P_{fr} could be largely increased by fabricating a microcavity with optimized parameters:

- (i) a lower quality factor (presently, $Q = \omega_0/(2\pi\gamma) = 5600$) allows reducing the two-photon absorption rate that scales like $1/\gamma^2$, while the polariton-phonon scattering rate scales like $1/\gamma$. Obviously, γ cannot be increased to arbitrarily large values as it must be low enough to conserve the strong coupling regime.

- (ii) Increasing the Rabi splitting $\hbar\omega_R$ should fully suppress the slow cooling mechanism in favor of the fast one. Indeed, phonons display a natural cutoff energy at $\Omega_{\mathrm{LO}}^{max}$ corresponding to the highest energy optical phonon state. If Ω_R amounts to twice $\Omega_{\mathrm{LO}}^{max}$, no phonon mode can scatter a polariton into the excitonic reservoir, and that, independently to the temperature. Such a suppression has been demonstrated already in a different context in a ZnO microcavity [37]. In our case, this regime would be reached for a Rabi splitting $\hbar\Omega_R = 2\hbar\Omega_{\mathrm{LO,ZnSe}}^{max} = 62 meV$, i.e. only about twice the current Rabi splitting.

Applying those adjustments and by removing the GaAs substrate of the cavity and thermally decoupling the active cooling region from the rest of the structure by etching brace holding the free standing cavity, one would obtain a sample that would be well suited for an experimental measurement of the temperature drop under polariton ASF cooling.

As further perspectives, the *fast* cooling process described in this chapter, thanks to its unusual dynamic opens up an experimental window on the out-of-equilibrium thermodynamics of phonons. Finally, polariton fluids has been shown to constitute an experimental model system to study the heat transport properties between a thermal bath and an out-of-equilibrium fluid.

General conclusion

The aim of the work presented in that manuscript was to study how polaritons interact with their solid state environment.

In the first chapter, we have shown that a ZnO one dimensional polariton condensate featuring an excitonic fraction of 97% is in the vanishing interaction regime. The influence of this 3% photonic dressing has been addressed, showing that the correlation length of the polaritons is at least one order of magnitude larger than the diffusion length of the bare excitons in ZnO. This last result combined with the very small Bohr radius featured by the exciton in ZnO are the key points of the ability of ZnO polaritons to enter in the quantum degeneracy regime even with such a high excitonic fraction. The time integrated first order spatial correlation function of the polariton condensate has been experimentally determined. The polariton condensate has been shown to feature a spatial coherence range of the order of the one observed in 2D polaritons with a 50% excitonic fraction. The obtained results coupled to a mean field driven dissipative model simulating the condensate allowed to understand that the influences of both polariton-polariton and exciton-polariton interactions are negligible as compared to the effect of disorder. The study of the influence of both the polariton lifetime and the disorder of the potential experienced by the condensate shown that the later has a strong impact on the spatial correlations, the one of the lifetime being negligible in the frame of the experiment.

In the second part we have shown as an experimental proof of principle a novel all optical mean to cool down a cavity exploiting the interactions between the polaritons and the phonons. The cooling mechanism is based on the polariton Anti Stokes Fluorescence, it features an outstanding bandwidth being able to remove phonons of arbitrary low energy and a dynamic which is as fast as the polariton lifetime. The mechanisms involved in the cooling process have been detailed and their relative efficiencies have been determined. The temperature dependency of the polariton ASF cooling efficiency has been studied, demonstrating that the optimum cooling power is situated arround 50K where the conventional optical cooling methods are disabled. The *fast* mechanism observed and

commented is specific to polaritons, its out of equilibrium nature has been shown to provide a larger cooling efficiency than the one expected for a at equilibrium coolant. The latter allows an experimental approach of the out of equilibrium thermodynamics of phonons.

As perspectives, The polariton gas has been shown to constitute an interesting system to study thermodynamics of an out of equilibrium fluid interacting with a thermal reservoir. The last point opens the way to the investigation of a blockade of the heat transfer in a polariton superfluid : the linear relation of dispersion of the superfluid polariton state reducing dramatically the number of available arrival states for ASF scattering of polaritons. The Zinc oxide microwires investigated in the first chapter, thanks to the high Rabi splitting they feature and to their very small thermal capacity would also be an ideal sample to implement the ASF strategy, by thermally decoupling them from the substrate, one might be able to measure the experimental drop of temperature of the lattice under ASF cooling.

Colophon

This thesis was made in LaTeX 2_ε using the "hepthesis" class.

Bibliography

[1] E. Becquerel, Comptes rendus hebdomadaires des séances de l'Académie des sciences / publiés... par MM. les secrétaires perpétuels, 1839.

[2] A. Einstein, Annalen der Physik **322**, 132 (1905).

[3] A. Einstein, Deutsche Physikalische Gesellschaft **18**, 318 (1916).

[4] T. H. Maiman, Nature **187**, 493 (1960).

[5] M. H. Anderson, J. R. Ensher, M. R. Matthews, C. E. Wieman, and E. A. Cornell, Science **269**, 198 (1995).

[6] K. B. Davis *et al.*, Physical Review Letters **75**, 3969 (1995).

[7] S. Bose, Zeitschrift f¨ur Physik **26**, 178 (1924).

[8] A. Einstein, Zweite Abhandlung , 3 (1925).

[9] P. Goy, J. M. Raimond, M. Gross, and S. Haroche, Physical Review Letters **50**, 1903 (1983).

[10] C. Weisbuch, M. Nishioka, A. Ishikawa, and Y. Arakawa, Physical Review Letters **69**, 3314 (1992).

[11] J. Kasprzak *et al.*, Nature **443**, 409 (2006).

[12] A. A. High *et al.*, Nature **483**, 584 (2012).

[13] M. Sheik-Bahae and R. I. Epstein, Physical Review Letters **92**, 247403 (2004).

[14] J. Zhang, D. Li, R. Chen, and Q. Xiong, Nature **493**, 504 (2013).

[15] D. S. Petrov, G. V. Shlyapnikov, and J. T. M. Walraven, Physical Review Letters **85**, 3745 (2000).

[16] F. London, Nature **141** (1938).

[17] L. Tonks, Physical Review **50**, 955 (1936).

[18] M. Girardeau, Journal of Mathematical Physics **1**, 516 (1960).

[19] B. Paredes *et al.*, Nature **429**, 277 (2004).

[20] S. Richard *et al.*, Physical Review Letters **91**, 010405 (2003).

[21] A. Imamoglu, R. J. Ram, S. Pau, and Y. Yamamoto, Physical Review A **53**, 4250 (1996).

[22] A. Amo *et al.*, Nature Physics **5**, 805 (2009).

[23] K. G. Lagoudakis *et al.*, Nature Physics **4**, 706 (2008).

[24] K. G. Lagoudakis *et al.*, Science **326**, 974 (2009).

[25] M. Sich *et al.*, Nature Photonics **6**, 50 (2012).

[26] A. Amo *et al.*, Science **332**, 1167 (2011).

[27] E. Wertz *et al.*, Nature Physics **6**, 860 (2010).

[28] M. Richard, J. Kasprzak, R. Romestain, R. André, and L. S. Dang, Physical Review Letters **94**, 187401 (2005).

[29] M. Wouters, I. Carusotto, and C. Ciuti, Physical Review B **77**, 115340 (2008).

[30] E. Wertz *et al.*, Physical Review Letters **109**, 216404 (2012).

[31] D. Tanese *et al.*, Physical Review Letters **108**, 036405 (2012).

[32] M. Wouters, T. C. H. Liew, and V. Savona, Physical Review B **82**, 245315 (2010).

[33] F. Manni *et al.*, Physical Review Letters **106**, 176401 (2011).

[34] F. Manni, K. G. Lagoudakis, R. André, M. Wouters, and B. Deveaud, Physical Review Letters **109**, 150409 (2012).

[35] A. Chiocchetta and I. Carusotto, EPL (Europhysics Letters) **102**, 67007 (2013).

[36] V. N. Gladilin, K. Ji, and M. Wouters, arXiv:1312.0452 [cond-mat] (2013), arXiv: 1312.0452.

[37] A. Trichet *et al.*, Physical Review B **83**, 041302 (2011).

[38] J.-S. Hwang *et al.*, Nanotechnology **22**, 475704 (2011).

[39] C. F. Klingshirn, *Semiconductor Optics*Graduate Texts in Physics (Springer Berlin Heidelberg, Berlin, Heidelberg, 2012).

[40] C. Klingshirn *et al.*, physica status solidi (b) **247**, 1424 (2010).

[41] M. Zamfirescu, A. Kavokin, B. Gil, G. Malpuech, and M. Kaliteevski, Physical Review B **65**, 161205 (2002).

[42] R. Shimada, J. Xie, V. Avrutin, u. ¨Ozg¨ur, and H. Morko§, Applied Physics Letters **92**, 011127 (2008).

[43] T.-C. L. Jun-Rong Chen, Applied Physics Letters **94**, 061103 (2009).

[44] F. Médard *et al.*, Physical Review B **79**, 125302 (2009).

[45] L. Sun *et al.*, Physical Review Letters **100**, 156403 (2008).

[46] J. M. Blatt, K. W. BÃ¶er, and W. Brandt, Physical Review **126**, 1691 (1962).

[47] S. Moskalenko, Soviet Physics-Solid State **4**, 199 (1962).

[48] D. Hulin, A. Mysyrowicz, and C. B. Ã la Guillaume, Physical Review Letters **45**, 1970 (1980).

[49] L. L. Chase, N. Peyghambarian, G. Grynberg, and A. Mysyrowicz, Physical Review Letters **42**, 1231 (1979).

[50] T. Guillet *et al.*, Applied Physics Letters **99**, 161104 (2011).

[51] C. Kittel, *Introduction to solid state physics*, 7th ed ed. (Wiley, New York, 1996).

[52] G. H. Wannier, Physical Review **52**, 191 (1937).

[53] J. Frenkel, Physical Review **37**, 17 (1931).

[54] W. S. Baer, Physical Review **154**, 785 (1967).

[55] H. Morkoç and Ozgur, *Zinc Oxide: Fundamentals, Materials and Device Technology* (Wiley-VCH Verlag GmbH & Co. KGaA, 2009).

[56] R. J. Elliott, Physical Review **108**, 1384 (1957).

[57] J. J. Hopfield, Physical Review **112**, 1555 (1958).

[58] A. Auffèves *et al.*, editors, *Strong light-matter coupling: from atoms to solid-state systems* (World Scientific, New Jersey, 2014).

[59] K. Hazu *et al.*, Journal of Applied Physics **96**, 1270 (2004).

[60] E. Mallet *et al.*, Physical Review B **87**, 161202 (2013).

[61] G. Pavlovic, G. Malpuech, and N. A. Gippius, Physical Review B **82**, 195328 (2010).

[62] Klingshirn K., *Zinc Oxide - From Fundamental Properties Towards Novel Applications*, Springer, berlin ed. .

[63] B. K. Meyer *et al.*, physica status solidi (b) **241**, 227 (2004).

[64] L. K. van Vugt *et al.*, Physical Review Letters **97**, 147401 (2006).

[65] P. Y. Yu and M. Cardona, *Fundamentals of Semiconductors - Physics and Materials Properties* .

[66] F. B. R Atanasov, Physical review. B, Condensed matter **50**, 14381 (1994).

[67] A. Amo, M. D. Martin, L. Vina, A. I. Toropov, and K. S. Zhuravlev, Journal of applied physics **101** (2007).

[68] R. André, D. Heger, L. S. Dang, and Y. Merle d'Aubigné, Journal of Crystal Growth **184**, 758 (1998).

[69] N. Cain *et al.*, Journal of Luminescence **75**, 269 (1997).

[70] G. Christmann *et al.*, Physical Review B **77**, 085310 (2008).

[71] K. Kornitzer *et al.*, Physical Review B **60**, 1471 (1999).

[72] K. Takahashi, A. Yoshikawa, and A. Sandhu, editors, *Wide bandgap semiconductors: fundamental properties and modern photonic and electronic devices* (Springer, Berlin ; New York, 2007).

[73] A. Trichet, *Polaritons unidimensionnels dans les microfils de Zno : vers la dégénérescence quantique dans les gaz de polaritons unidimensionnels*, PhD thesis, Université de Grenoble, 2012.

[74] T. Nobis, E. M. Kaidashev, A. Rahm, M. Lorenz, and M. Grundmann, Physical Review Letters **93**, 103903 (2004).

[75] A. Trichet, F. Médard, J. Zúniga-Pérez, B. Alloing, and M. Richard, New Journal of Physics **14**, 073004 (2012).

[76] G. Rupper, N. H. Kwong, and R. Binder, Physical Review Letters **97**, 117401

(2006).

[77] M. Sheik-Bahae and R. I. Epstein, Nature Photonics **1**, 693 (2007).

[78] H. Gauck, T. H. Gfroerer, M. J. Renn, E. A. Cornell and K. A. Bertness, Applied Physics A , 143 (1997).

[79] E. Finkeissen, M. Potemski, P. Wyder, L. Vina and G. Weimann, Applied Physics Letters **75**, 1258 (1999).

[80] M. I. Dyakonov, editor, *Spin physics in semiconductors*, Springer series in solid-state sciences No. 157 (Springer, Berlin, 2008).

[81] RÃºda, H.E, *Widegap IIâVI Compounds for Opto-electronic Applications | Springer* .

[82] K. Sebald *et al.*, Applied Physics Letters **100**, 161104 (2012).

[83] S. Klembt, *II-VI-basierte MikrokavitÃten f¨ur den blau-violetten Spektralbereich: Lasing im Bereich schwacher und starker Kopplung / von Sebastian Klembt* (mbv, Mensch-und-Buch-Verl., Berlin, 2014).

[84] K. F. Sebastian Klembt, Journal of Crystal Growth **378**, 270 (2013).

[85] H. L. S. K. Zhang, Journal of Applied Physics **101**, 023111 (2007).

[86] W. Langbein *et al.*, Physical Review B **75**, 075323 (2007).

[87] A. Kavokin, G. Malpuech, and M. Glazov, Physical Review Letters **95**, 136601 (2005).

[88] C. Leyder *et al.*, Nature Physics **3**, 628 (2007).

[89] F. Tassone, C. Piermarocchi, V. Savona, A. Quattropani, and P. Schwendimann, Physical Review B **56**, 7554 (1997).

[90] G. Rozas *et al.*, Physical Review Letters **102**, 015502 (2009).